ISA Transactions 172 (2026) 83–104

Contents lists available at ScienceDirect

ISA Transactions

journal homepage: www.elsevier.com/locate/isatra

Research article

Design of a virtual sensing methodology for vehicle ride and comfort applications

Mario Barbaro [a], Guido Napolitano Dell'Annunziata [a], Miguel Ángel Naya [b], Antonio J. Rodríguez [b], Aleksandr Sakhnevych [a,*], Emilio Sanjurjo [b], Francisco J. González [b]

[a] Department of Industrial Engineering, University of Napoli Federico II, Naples 80125, Italy
[b] Laboratorio de Ingeniería Mecánica, CITENI, Campus Industrial Ferrol, Universidade da Coruña, Ferrol, 15403, Spain

HIGHLIGHTS

- A virtual sensing methodology is developed to estimate macroscopic road obstacles using acceleration, angular velocity and suspension deflection measurements with a reduced-order vehicle model. The logic aims to perform the simultaneous estimation of the out-of-road-plane vehicle and tyre motions.
- Validation is performed using synthetic data from a 14-dof multibody vehicle model.
- The reduced-order model explicitly accounts for suspension constraint effects in tyre and chassis dynamics through a simplified formulation: starting from the multibody model as a baseline, nonlinear variations in the dynamic equations—due to instantaneous constraint configurations—are quantitatively analysed over a wide operating domain and approximated using analytical functions.
- A nonlinear Kalman filter is designed to optimize estimation accuracy and ensure full state observability. A sensitivity analysis is then carried out to test the influence of the filter parameters, particularly the noise covariance matrix, on the observer's performance. The robustness of the observer to parameter errors is tested, as well as the impact of the measurement noise on the estimation accuracy.

ARTICLE INFO

Keywords:
Vehicle state estimator
Ride and comfort
Multibody modelling
Suspension constraints
Virtual sensing

ABSTRACT

Accurate real-time estimation of the instantaneous vehicle state plays a crucial role in modern automotive research, both in the state diagnostics and anomaly detection and in the design and development of advanced control systems and onboard monitoring strategies. In particular, accurate knowledge of chassis motion and wheel dynamics in response to road disturbances is essential for advanced control strategies aimed at simultaneously enhancing ride quality and handling. However, the road profile represents an unmeasured and highly variable input, often requiring complex and costly sensors such as LiDAR for direct observation: this motivates the development of virtual sensing approaches capable of inferring road irregularities from standard onboard sensors.

This work presents a novel state observer based on an Extended Kalman Filter (EKF) architecture for the online estimation of road-induced excitations and key vehicle dynamic quantities, including chassis out-of-plane motions, suspension displacements, and tyre-loaded radii. The observer relies on a computationally efficient 7-degree-of-freedom vehicle model, analytically derived through a streamlined multibody formulation, and validated against a high-fidelity multibody reference model under two sensor configurations, both limited to signals typically available in mass-produced vehicles. The results achieved, even when using high-noise measurements, are encouraging for further applications in real-world virtual sensing scenarios.

1. Introduction

The contemporary automotive industry is increasingly moving towards a smart mobility paradigm, driven by the integration of Advanced Driver Assistance Systems (ADAS) [1,2], designed to reduce road accidents and increase vehicle automation levels, making autonomous driving accessible on a large scale. In this context, where an accurate

* Corresponding author.
Email addresses: mario.barbaro@unina.it (M. Barbaro), guido.napolitanodellannunziata@unina.it (G. Napolitano Dell'Annunziata), miguel.naya@udc.es (M.Á. Naya), antonio.rodriguez.gonzalez@udc.es (A.J. Rodríguez), ale.sak@unina.it (A. Sakhnevych), emilio.sanjurjo@udc.es (E. Sanjurjo), f.gonzalez@udc.es (F.J. González).

https://doi.org/10.1016/j.isatra.2026.03.007
Received 7 August 2025; Received in revised form 5 March 2026; Accepted 5 March 2026
Available online 7 March 2026

knowledge of the instantaneous vehicle kinematics and dynamics is required, a crucial role is played by the development of virtual sensing algorithms, which have become essential due to the impossibility of directly measuring certain key quantities, such as side-slip angle, grip level, tyre forces, and tyre slip ratios, without relying on high-end sensors that are unsuitable for mass-produced vehicles. In this regard, various approaches have been developed in the literature, employing vehicle state observers, usually based on Extended Kalman Filter (EKF), Unscented Kalman Filter (UKF) or other architectures [3], designed to estimate the unmeasured quantities using sensors commonly available in passenger vehicles, such as accelerometers, gyroscopes, wheel speed and wheel steering sensors [4].

In particular, model-based strategies are commonly employed in vehicle handling applications, as the trade-off between their predictability and computational efficiency makes them ideal for effective integration into control systems such as ABS and ESP [5]. Various model-based approaches can be found in the current literature. Kinematic observers, based on kinematic equations and onboard measurements of linear acceleration and angular velocity [6,7], do not require calibration of tyre or vehicle models and remain robust under transient and nonlinear manoeuvres. However, they become unobservable when yaw rate tends to zero, are highly sensitive to sensor noise, and cannot estimate tyre–road interaction variables. Dynamic approaches address these limitations by implementing vehicle equilibrium equations and tyre models to estimate contact-patch forces [8–10]. These approaches are more accurate but rely on steady-state assumptions, reducing reliability during transient manoeuvres; therefore, they are often combined with kinematic estimators in hybrid schemes [11–13]. To further enhance accuracy, more recent works integrate multibody vehicle models into KF-based observers [14,15], employing efficient numerical procedures such as look-up-table-based formulations [16] to allow real-time capability. These methods explicitly account for suspension constraints, accurately modelling wheel-orientation variations and transient effects on vertical tyre loads, but rely on an accurate knowledge of vehicle subsystems' parameters.

Considering that the instantaneous road profile significantly influences the mentioned model-based estimation techniques, these are often integrated with adaptive schemes that incorporate the onboard estimation of road slope and banking, which are crucial for compensating acceleration signals [17,18]. However, the same focus is not dedicated to the online estimation of local road irregularities, which are typically neglected in estimators conceived for handling applications and primarily focused on vehicle dynamics within the road plane. This represents a significant limitation, as ride-related phenomena play a crucial role in the real-time evolution of tyre and vehicle dynamics by affecting slip ratios, vertical loads, and chassis orientation [19]. Moreover, ride-related state variables are expected to play an increasingly important role in the development of modern control systems, which aim not only to ensure vehicle manoeuvrability but also to preserve the health and comfort of both the driver and passengers [20–22]. In this regard, the current literature approaches for onboard estimation of road irregularities are limited to approximate formulations, usually relying on quarter-car models [23–25], without observing the full system response and neglecting the influence of instantaneous suspension constraints. Other methodologies employ dedicated sensing systems, such as LiDAR [26–28], which, however, require costly instrumentation and are difficult to implement in standard production vehicles.

To address the aforementioned limitations in the state of the art approaches, this article proposes the design of a virtual sensing logic for the onboard detection of large-amplitude road irregularities, through a full-vehicle formulation, allowing to estimate the overall response of the system and without relying on high-end sensors. The proposed method employs a highly efficient EKF physical model-based approach that simultaneously estimates the out-of-plane dynamics of the vehicle, suspensions, and tyre states, excited by the road irregularities. The time-update equations of the estimator rely on a simplified model designed to provide results comparable to those of a multibody vehicle model, which, despite its higher accuracy and level of detail, is difficult to parameterise without specific vehicle data and exhibits strong nonlinearity that can degrade performance within an EKF filter, or other estimators with contained complexity; therefore, a trade-off was made by sacrificing some model accuracy in favour of reduced complexity, relying on the filter's feedback to compensate for residual modelling errors.

A detailed multibody vehicle model was used as a reference to generate data for both validating the proposed approach and modelling the sensor signals employed in the estimation logic. These data were obtained by simulating the vertical interaction between the tyre, modelled with radial stiffness and damping, and an equivalent contact point representing the road unevenness. Simulations were repeated assuming various unevenness profiles, changing the time histories of the equivalent contact point consequently. Furthermore, the simulation outputs used in the measurement update equations were additionally corrupted with white noise to reproduce realistic sensor disturbances, typical of the real vehicle system.

Regarding the employed measurements, two different sensing configurations were implemented. The first relies solely on acceleration and angular velocity sensors, without requiring suspension deflection measurements. This represents an innovative aspect compared to multibody-based estimators in the existing literature and offers clear advantages in terms of large-scale applicability. The second configuration, which includes suspension measurements, was implemented and compared with the first, under various road irregularity conditions, analysing how the absence of such additional signals could affect the robustness of the estimator and its potential application domain.

The structure of the paper is as follows:

- Section 2 presents the implementation of the reference multibody vehicle model, developed using the natural coordinates methodology, and reports the set of simulations performed for data collection.
- Section 3 describes the design of the simplified model employed in the time-update equations of the estimator. The model is validated through open-loop simulations by comparing its results with those of the reference model.
- Section 4 illustrates the architecture of the estimation logic in both the two considered measurement configurations, providing justification for the implementation strategies adopted to ensure the observability of the system and to enhance the reliability of the estimation.
- Section 5 presents a comprehensive analysis of the estimators' performance under the different investigated operating conditions, including an additional validation phase in which random perturbations are introduced into the model parameters to assess the robustness of the observer to modelling uncertainties. Moreover, a sensitivity analysis is carried out to evaluate how variations in both filter tuning parameters and measurement noise levels influence the overall estimation accuracy.
- Finally, a concluding Section 6 summarizes the main findings of the work and outlines potential future developments.

2. Reference vehicle model implementation for data collection

Given the prototypical nature of the estimator, validation was conducted in a fully controlled simulation environment to eliminate typical uncertainties found in experimental data, such as driver behaviour, measurement errors, and environmental conditions. This led to the implementation of an accurate reference vehicle model, used to generate synthetic data both as an ideal benchmark for validating the proposed virtual sensing logic and to simulate onboard sensor signals

by artificially adding noise. The reference model was designed to meet a dual requirement: on the one hand, it had to realistically reproduce the behaviour of a real vehicle under the explored operating conditions; on the other hand, it had to avoid including macroscopic physical phenomena that are not taken into account within the estimation logic.

For this reason, the assumption of rigid constraints was adopted. In fact, with respect to the first requirement, compliance effects are more relevant in vehicle ride behaviour at intermediate-high frequencies, whereas this preliminary study focuses on the dominant out-of-plane vehicle and tyre dynamics, operating in the frequency range relevant to primary ride [29]. Regarding the second requirement, including bushing compliances in the estimator would increase the number of degrees of freedom and the overall complexity, compromising algorithmic efficiency and exceeding the intended scope of the estimation strategy. Conversely, introducing compliances only in the reference model would create inconsistencies with the estimator, potentially introducing unmodelled dynamic effects that affect the reference data but are not captured by the estimator. This would represent a source of error that compromises an objective evaluation of the estimator's performance. Therefore, inclusion of more detailed vehicle models will be object of further developments of this work, following the completion of this preliminary validation.

Furthermore, it is important to highlight that the reference model, described in detail in the current section, is not implemented within the estimator. As will be discussed in Section 3, the estimation logic instead relies on a simplified model which, although less detailed, is derived using the reference model as a baseline and built based on the same dominant macroscopic physical principles.

2.1. Modelling hypotheses and implementation

Therefore, a multibody vehicle model was implemented as a reference within a MATLAB-Simulink simulation environment, adopting the modelling approach relying on natural coordinates [30,31], commonly employed in modelling closed-loop constrained systems, such as suspensions. The vehicle chassis was modelled as a 6-dof rigid mass, while the steering system was represented by a data-driven kinematic constraint relating steering wheel angle to rack displacement. However, since only straight-line manoeuvres were considered in this study, the steering degree of freedom was omitted. The tyre–suspension system consisted of rigid bodies connected via rigid joints, with tyre-road interaction modelled using a linear vertical tyre model; horizontal forces were neglected in this phase. Both front and rear suspensions were modelled as double wishbone configurations, composed of rigid bodies shown in Fig. 1. Each body is defined by a set of natural coordinates (Fig. 1), including points and unit vectors used to impose constraints between bodies and to define local reference triads necessary for the calculation of the mass matrix [30,31]. Additional natural coordinates correspond to the wheel rotation angles and distances between the strut extremities (lower and upper mounts), which are necessary to define suspension forces.

The equations of motion are implemented according to the R-matrix formulation [32], employing a Runge-Kutta integration method, based on trapezoidal rule [3,33], with a time step of 1 ms. The R-matrix transformation allows the system to be expressed in terms of a reduced set of independent coordinates, Eqs. (1) and (2), which include the position of the vehicle's centre of gravity $(x_{CG}; y_{CG}; z_{CG})$, the Euler angles defining the chassis orientation $(\phi; \theta; \psi)$, the vertical displacements of the wheel centres $(z_{FL}; z_{FR}; z_{RL}; z_{RR})$, and the rotational angles of the wheels $(\phi_{FL}; \phi_{FR}; \phi_{RL}; \phi_{RR})$:

$$\mathbf{M}_{\text{ref}}\,\ddot{\mathbf{z}}_{\text{ref}} = \mathbf{Q}_{\text{ref}} \tag{1}$$

$$\mathbf{z}_{\text{ref}} = [x_{CG}; y_{CG}; z_{CG}; \phi; \theta; \psi; z_{FL}; z_{FR}; z_{RL}; z_{RR}; \phi_{FL}; \phi_{FR}; \phi_{RL}; \phi_{RR}] \tag{2}$$

where $\mathbf{M}_{\text{ref}}$ and $\mathbf{Q}_{\text{ref}}$ are obtained through a transformation of the mass matrix $\bar{\mathbf{M}}$ and the force vector $\bar{\mathbf{Q}}$, both originally defined in natural

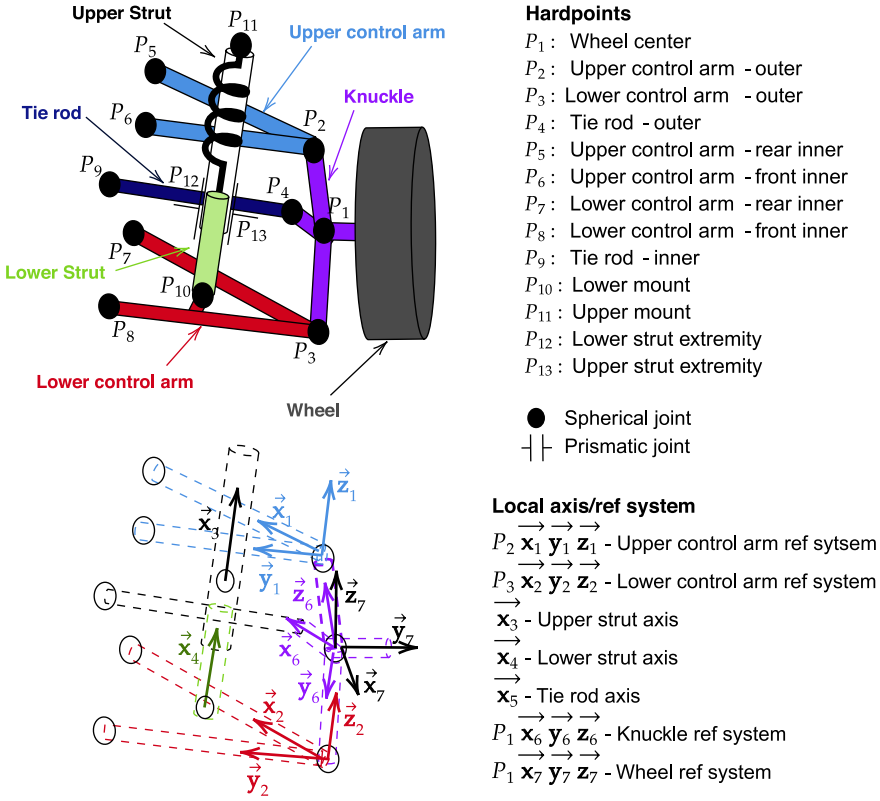

Fig. 1. Schematic representation of the constraints and of the local reference system for each rigid body.

coordinates [30], as shown in Eqs. (3) and (4):

$$\mathbf{M}_{\text{ref}} = \mathbf{R}_{\text{ref}}^{\text{T}} \bar{\mathbf{M}} \mathbf{R}_{\text{ref}} \tag{3}$$

$$\mathbf{Q}_{\text{ref}} = \mathbf{R}_{\text{ref}}^{\text{T}} (\bar{\mathbf{Q}} - \bar{\mathbf{M}} \dot{\mathbf{R}}_{\text{ref}} \dot{\mathbf{z}}_{\text{ref}}) \tag{4}$$

where the R-matrix $\mathbf{R}_{\text{ref}}$ and its time derivative $\dot{\mathbf{R}}_{\text{ref}}$ are computed in each iteration, once the position problem and the velocity problem are solved. The generalized force vector in natural coordinates can be expressed as a combination of three contributions, respectively related to gravity, suspensions and tyres, Eq. (5).

$$\bar{\mathbf{Q}} = \bar{\mathbf{Q}}^{\text{g}} + \bar{\mathbf{Q}}^{\text{t}} + \bar{\mathbf{Q}}^{\text{s}} \tag{5}$$

The first force vector, $\bar{\mathbf{Q}}^{\text{g}}$, is constant and calculated by applying the corresponding weight force at the centre of mass of each rigid body and computing the resulting vector as the superposition of all contributions. The formulation of each component depends on the position of the rigid body's centre of mass relative to the origin of the local reference frame, and on the linear combination used to define this local frame as a function of the system's natural coordinates [30].

The second force vector, $\bar{\mathbf{Q}}^{\text{t}}$, represents the four vertical tyre forces, modelled as linearly dependent on the vertical displacement between the wheel centre and the tyre-road contact point, Eq. (6). These forces are applied to the natural coordinates associated with the vertical positions of the wheel centres, as they are assumed to act directly on these points.

$$\bar{\mathbf{Q}}^{\text{t}} = \begin{pmatrix} \dots \\ F_{z_{FL}} \\ \dots \\ F_{z_{FR}} \\ \dots \\ F_{z_{RL}} \\ \dots \\ F_{z_{RR}} \\ \dots \end{pmatrix} \quad \text{with } F_{z_i} = K_t(r_u - r_{l_i}) + B_t(\dot{z}_{r_i} - \dot{z}_i) \quad \text{and } r_{l_i} = z_i - z_{r_i} \tag{6}$$

where K_t is the tyre stiffness, B_t is the tyre damping coefficient, r_u is the unloaded radius and z_i and z_{r_i} are the wheel centre and contact point vertical positions, respectively.

Regarding the third vector, $\bar{\mathbf{Q}}^{\text{s}}$, the four suspension forces, proportional to both suspension displacement and velocity, Eq. (7), are applied to the natural coordinates corresponding to the distances between the suspension endpoints, consistent with the methodology adopted for modelling actuators in natural coordinates.

$$\bar{\mathbf{Q}}^{\text{s}} = \begin{pmatrix} \dots \\ F_{s_{FL}} \\ \dots \\ F_{s_{FR}} \\ \dots \\ F_{s_{RL}} \\ \dots \\ F_{s_{RR}} \\ \dots \end{pmatrix} \quad \text{with } F_{s_i} = -K_s(\delta l_i - \delta l_{0_i}) - B_s \dot{\delta l}_i \tag{7}$$

where K_s, B_s, δl_{0_i} are suspension stiffness, damping coefficient and natural length, respectively, while δl_i and $\dot{\delta l}_i$ represent the suspension distance and its time derivative.

Since the development of the reference model is not the main focus of the work, the details of natural coordinates modelling are not included here; these can be found in the cited literature [30,32]. However, to facilitate the understanding, a schematic representation of the simulation workflow is provided by Fig. 2. It involves the computation of the R-matrix and its time-derivative, starting from the vector of natural coordinates and their time derivatives. Then, the equation of motion is formulated, and the acceleration of the independent coordinates is computed. Following the numerical integration, the natural coordinates, both at position and velocity levels, are computed from the independent coordinates, by solving the position and velocity problems represented through the functions f_{pp} and f_{vp} respectively. The road heights $\mathbf{z}_{\text{r}}$ and their time derivatives $\dot{\mathbf{z}}_{\text{r}}$ are provided as input to the model, specifically for the calculation of the force vector in natural coordinates.

The parameters adopted for the implementation of the reference multibody model are reported in Tables 1–3. Table 1 lists the coordinates of the suspension hardpoints, defined with respect to the vehicle reference frame, thus describing the geometry of both the front-left and rear-left suspensions (the right suspensions are symmetric). Table 2 reports the mass and inertia properties of the vehicle chassis, suspension assemblies, and wheels, expressed in their respective local reference frames. Finally, Table 3 summarizes the mechanical properties adopted for the suspension and tyre models, including stiffness, damping, the natural length (for the suspension), and the unloaded radius (for the tyres).

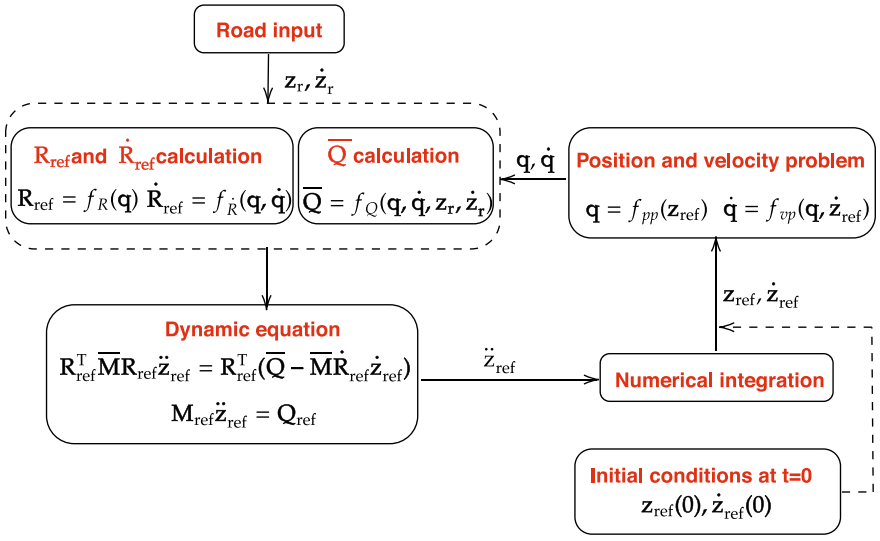

Fig. 2. Simulation workflow of multibody dynamic modelling in natural coordinates.

Table 1
Suspension hardpoints coordinates in the vehicle reference frame.

Hardpoint	Front-left			Rear-left		
	X [mm]	Y [mm]	Z [mm]	X [mm]	Y [mm]	Z [mm]
Wheel centre	−1233	−760	−120	1327	−797	−100
LCA front	−1433	−400	−270	1127	−400	−210
LCA outer	−1233	−750	−320	1327	−750	−260
LCA rear	−1033	−450	−265	1527	−450	−205
UCA front	−1133	−450	105	1427	−450	125
UCA outer	−1193	−675	105	1367	−675	125
UCA rear	−983	−490	110	1577	−490	130
Tierod inner	−1033	−400	−120	1527	−400	−100
Tierod outer	−1083	−750	−120	1477	−750	−100
Strut lower mount	−1233	−600	−270	1327	−600	−250
Strut top mount	−1193	−500	230	1367	−500	250

Table 2
Mass and inertia properties of full-vehicle model components.

Component	m [kg]	I_{xx} [kg m^2]	I_{yy} [kg m^2]	I_{zz} [kg m^2]
Vehicle chassis	1450	200	500	600
Front suspension	6.5	0.383	0.227	0.264
Rear suspension	14.4	1.202	0.466	0.853
Front wheel	25.00	0.800	1.000	0.800
Rear wheel	25.00	0.800	1.000	0.800

Table 3
Mechanical properties of suspensions and tyres.

Component	Suspension			Tyre		
	K_s [N/m]	B_s [Ns/m]	δl_0 [m]	K_t [N/m]	B_t [Ns/m]	r_u [m]
Front axle	50,000	3000	0.6215	210,000	500	0.3
Rear axle	50,000	3000	0.6535	210,000	500	0.3

2.2. Design of simulations for data collection

The simulation campaign was specifically designed to collect qualitatively representative data with two main purposes: validation and sensitivity analysis of the virtual sensing algorithm and supporting the design phase of the reduced-order model (described in the following section), through a comprehensive investigation of the variation of the terms in the equations of motion across a representative operating domain of the vehicle. It has to be highlighted that, given the approximate nature of the reference model, the focus is not on accurately replicating real-world data, but on generating different and physically plausible scenarios that are able to excite the key dynamics relevant in the estimation process.

The simulated scenario considers a straight-line passage over a road irregularity, including simulations with both bumps and potholes by defining a variable vertical height of the contact point between the tyre and the ground, with a specific time history profile modelling the tyre–road impact phenomenon (Fig. 3). It is important to underline that the applied input does not represent the real geometric profile of the road, but rather the vertical displacement of an equivalent contact point between the tyre and the ground, representative of a continuously enveloping single-contact modelling approach, widely adopted to describe the tyre–road interaction on road unevenness, accounting for the effective contact patch extension [34].

The variation of the described contact point height is defined as a half-sinusoidal function in the spatial domain, with a specified maximum height h and length l, which is then converted into the time domain based on the assumed vehicle speed. As shown in Fig. 3, this conversion accounts for the time-domain shifting of the unevenness between the front and rear axles, which occurs as a function of both the vehicle speed v_x and the wheelbase a of the modelled vehicle, reflecting the

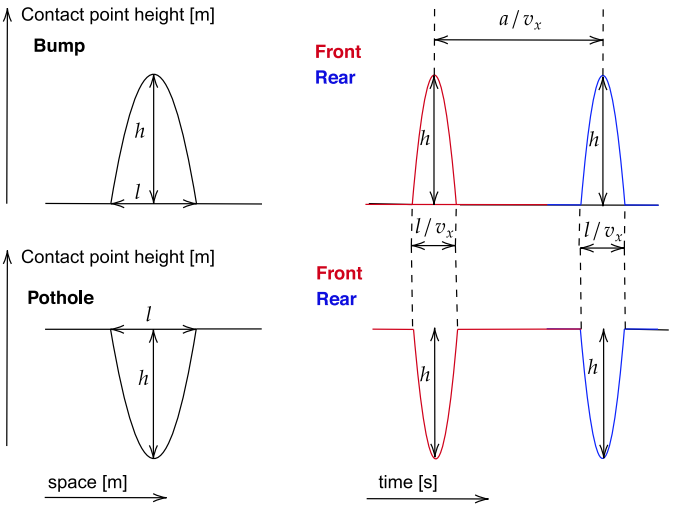

Fig. 3. Contact point height variation defined in space and time domains.

Table 4
Simulation campaign operating conditions.

v_x [m/s]			h [m]		l [m]	
5.0	7.5	10.0	0.05	0.10	1.00	1.25

vehicle's forward motion. As illustrated in the figure, two types of irregularities were modelled, representing the vehicle passing respectively over a bump or a pothole, by defining a half-sine profile with either positive or negative sign.

As reported in Table 4, the synthetic dataset was constructed by combining three vehicle speeds, two maximum heights, and two lengths of the imposed road profile. For each combination of operating conditions, the simulation was performed three times: once with the same profile applied to both left and right wheels, and twice more with the profile applied to either the left or the right side only, in order to simulate both symmetric and asymmetric responses. Furthermore, the entire simulation matrix was performed twice to account for both types of road irregularities considered in this study: a positive half-sine profile representing a bump, and a negative half-sine profile representing a pothole.

As part of the simulation framework, simulated sensors to be employed in the consequent state observer were modelled too, by specifically selecting certain output signals from the simulation and additionally imposing white noise, whose characteristics reflect the ones of real measurements. Indeed, the modelled sensors include:

- suspension deflection sensors, represented through the time histories of four natural coordinates from the multibody model corresponding to distances between top and lower mounts of the suspension spring;
- angular velocity measurements (pitch rate and roll rate), emulating signals from an inertial measurement unit (IMU). These simulation outputs were calculated within the vehicle's local reference frame, accounting for the chassis orientation through the Euler angles, as described in previous literature [14];
- linear acceleration measurements also modelled in the local sensor frame, including the effects of both sensor orientation and gravitational acceleration [14].

The noise parameters and sample frequencies adopted are summarized in Table 5, inheriting the imposed values from the previously published work [14].

Table 5
Characteristics of modelled sensors.

Sensor	Measurement unit	Frequency [Hz]	Noise
IMU accelerometer	m/s^2	250	0.45
IMU gyroscope	rad/s	250	0.011
Suspension displacement	m	250	0.01

3. Reduced-order model design

As previously mentioned, the multibody model described in Section 2 is used not only as a reference for validating the proposed state observer but also as a basis for designing the simplified model employed in the estimator. The aim was to derive a reduced formulation, neglecting some non-linearities, involving fewer parameters, and being suitable for real-time execution. In this regard, while a detailed multibody vehicle model can be integrated in real-time into embedded systems through efficient integration techniques [16] and may represent an optimal solution in terms of accuracy, its strongly non-linear state evolution can negatively impact the performance of the chosen Extended Kalman Filter (EKF) and of alternative filters with low nonlinearity, whose effectiveness depends on the ability to locally linearize the system dynamics around the current state. Moreover, full parameterisation of such a model requires detailed knowledge of the suspension geometry, the inertial properties of each rigid body, and the definition of their respective local reference frames.

Consequently, a series of simplification steps, which are going to be described in more detail in the following section, was carried out. In particular, the approximations introduced were aimed, first, at reducing the number of degrees of freedom considered in the model, and, beyond that, at neglecting additional coupling effects in the system dynamics, specifically by removing selected off-diagonal terms from the mass matrix and velocity-dependent constraint forces. Additionally, the variability of the suspension constraints was approximated by neglecting the influence of the chassis orientation, and defining the constraints in each corner as function of the respective suspension displacement, through simplified analytical functions. This allows to simplify the computation of the mass matrix and the force vector in independent coordinates, and the post-processing calculation of dependent variables.

The resulting approximated model, based on polynomial relationships between the terms of the differential equations and the instantaneous system state, is highly suitable for integration within an EKF logic and is easier to parameterise when vehicle properties are partially or entirely unknown. These advantages are expected to be crucial for future developments, aimed at avoiding excessively nonlinear filters (such as second-order EKF or particle filters) and for applications to instrumented vehicles for which detailed information is not available.

As a first step, the initial dynamic formulation, which included 14 state variables, was simplified by removing the degrees of freedom not relevant to the objectives of this work, specifically the wheel rotations and the in-plane (Oxy) chassis motions, resulting in a model that includes only the 7 degrees of freedom commonly considered in ride applications [19]. Therefore, seven constraint equations were introduced by assigning constant values to these variables, resulting in a system with seven degrees of freedom, defined by the following Eqs. (8)–(11), whose variables have been previously defined in the Eq. (2):

$$\mathbf{z} = [z_{CG}; \phi; \theta; z_{FL}; z_{FR}; z_{RL}; z_{RR}] \tag{8}$$

$$\mathbf{M}\ddot{\mathbf{z}} = \mathbf{Q} \tag{9}$$

$$\mathbf{M} = \mathbf{R}^{\mathrm{T}}\,\bar{\mathbf{M}}\,\mathbf{R} \tag{10}$$

$$\mathbf{Q} = \mathbf{R}^{\mathrm{T}}(\bar{\mathbf{Q}} - \bar{\mathbf{M}}\dot{\mathbf{R}}\dot{\mathbf{z}}) \tag{11}$$

where $\mathbf{M}$ and $\mathbf{Q}$ are obtained through the R-matrix based transformation of $\bar{\mathbf{M}}$ and $\bar{\mathbf{Q}}$ applied while accounting for the additional seven constraints. Therefore, the designed simplified model also presents a 7-dof model-based formulation, as reported in Eq. (12):

$$\mathbf{M}_{\mathrm{r}}\ddot{\mathbf{z}} = \mathbf{Q}_{\mathrm{r}} \tag{12}$$

where $\mathbf{M}_{\mathrm{r}}$ corresponds to a mass matrix whose components are defined as function of the instantaneous state of the system and $\mathbf{Q}_{\mathrm{r}}$ is defined by neglecting velocity-dependent constraint forces ($\bar{\mathbf{M}}\dot{\mathbf{R}}\dot{\mathbf{z}}$), and by considering $\mathbf{Q}_{\mathrm{r}}$ as a combination of three force vectors, related to gravity, suspensions and tyres, Eq. (13), as well as the original vector in natural coordinates.

$$\mathbf{Q}_{\mathrm{r}} = \mathbf{Q}_{\mathrm{r}}^{\mathrm{g}} + \mathbf{Q}_{\mathrm{r}}^{\mathrm{s}} + \mathbf{Q}_{\mathrm{r}}^{\mathrm{t}} \tag{13}$$

This simplification is considered acceptable for the case study addressed in this work, which focuses on straight-line simulated manoeuvres, where gyroscopic effects and other velocity-dependent contributions are negligible. However, in future developments involving cornering conditions, such effects are expected to play a more significant role and they will need to be reintroduced into the model in a simplified form. The computation of the force components in Eq. (13) and of the mass matrix will be described in the following subsections.

Regarding the last step of the workflow, which includes the calculation of the dependent coordinates, it has been simplified by considering only the dependent coordinates necessary for defining the approximated terms appearing in Eq. (12), and linearizing their computation from the independent coordinates, as will be subsequently described in detail.

3.1. Reduced forces' vector modelling

Considering the 7-dof formulation in natural coordinates, the non-approximated expressions of the three force components in independent coordinates can be defined as follows:

$$\mathbf{R}^{\mathrm{T}}\bar{\mathbf{Q}} = \mathbf{R}^{\mathrm{T}}\bar{\mathbf{Q}}^{\mathrm{g}} + \mathbf{R}^{\mathrm{T}}\bar{\mathbf{Q}}^{\mathrm{s}} + \mathbf{R}^{\mathrm{T}}\bar{\mathbf{Q}}^{\mathrm{t}} \tag{14}$$

Regarding the first term, although $\bar{\mathbf{Q}}^{\mathrm{g}}$ is constant, it is important to emphasize that, compared to the other force vectors of the equation, it contains a significantly higher number of non-zero components. This is because the gravity acts to all the rigid bodies in the system, resulting in force components applied on all the natural coordinates associated with the vertical positions of their centres of gravity [32]. For this reason, a non-approximated computation in independent coordinates would involve a linear combination of many constant terms multiplied by the corresponding coefficients of the R-matrix, which in turn would need to be expressed as functions of the system state, since they change with the instantaneous constraints. To reduce the complexity of the equations, the term $\mathbf{R}^{\mathrm{T}}\bar{\mathbf{Q}}^{\mathrm{g}}$ has been assumed constant with respect to the state and evaluated by computing the R-matrix at static equilibrium on a flat road, as expressed in Eq. (15). This simplification introduces an approximation across all operating conditions, except for static equilibrium, where the expression remains exact.

$$\mathbf{Q}_{\mathrm{r}}^{\mathrm{g}} = \mathbf{R}_{sl}^{\mathrm{T}}\bar{\mathbf{Q}}^{\mathrm{g}} \tag{15}$$

The forces related to tyre-road interaction $\bar{\mathbf{Q}}^{\mathrm{t}}$ are applied to natural coordinates corresponding to independent coordinates, specifically the wheel centre heights. Therefore, the exact solution of the term $\mathbf{R}^{\mathrm{T}}\bar{\mathbf{Q}}^{\mathrm{t}}$ is constituted by the four tyre forces F_{z_i} directly applied to the respective degrees of freedom of interest, and its simplicity allows avoiding further approximation:

$$\mathbf{Q}_{\mathrm{r}}^{\mathrm{t}} = \begin{pmatrix} 0 \\ 0 \\ 0 \\ F_{z_{FL}} \\ F_{z_{FR}} \\ F_{z_{RL}} \\ F_{z_{RR}} \end{pmatrix} \tag{16}$$

Regarding the suspensions' forces, they affect all the involved degrees of freedom, since they act both on the chassis and on the wheels' bodies. Therefore, all the components are going to be separately analysed, starting from the exact formulation involving the R-matrix coefficients and the suspensions' forces vector in natural coordinates:

$$\mathbf{Q}^{s}_{\text{exact}} = \mathbf{R}^{T}\bar{\mathbf{Q}}^{s} \tag{17}$$

The R-matrix coefficient $\mathbf{R}^{T}(i,j)$ corresponds to the velocity of the j-th natural coordinate when the velocity of the i-th independent coordinate is one and the others are equal to zero. Therefore, the Eq. (17) can be decomposed as follows:

$$\mathbf{Q}^{s}_{\text{exact}}(1,1) = F_{s_{FL}}\frac{\partial \delta l_{FL}}{\partial z_G} + F_{s_{FR}}\frac{\partial \delta l_{FR}}{\partial z_G} + F_{s_{RL}}\frac{\partial \delta l_{RL}}{\partial z_G} + F_{s_{RR}}\frac{\partial \delta l_{RR}}{\partial z_G} \tag{18}$$

$$\mathbf{Q}^{s}_{\text{exact}}(2,1) = F_{s_{FL}}\frac{\partial \delta l_{FL}}{\partial \phi} + F_{s_{FR}}\frac{\partial \delta l_{FR}}{\partial \phi} + F_{s_{RL}}\frac{\partial \delta l_{RL}}{\partial \phi} + F_{s_{RR}}\frac{\partial \delta l_{RR}}{\partial \phi} \tag{19}$$

$$\mathbf{Q}^{s}_{\text{exact}}(3,1) = F_{s_{FL}}\frac{\partial \delta l_{FL}}{\partial \theta} + F_{s_{FR}}\frac{\partial \delta l_{FR}}{\partial \theta} + F_{s_{RL}}\frac{\partial \delta l_{RL}}{\partial \theta} + F_{s_{RR}}\frac{\partial \delta l_{RR}}{\partial \theta} \tag{20}$$

$$\mathbf{Q}^{s}_{\text{exact}}(4,1) = F_{s_{FL}}\frac{\partial \delta l_{FL}}{\partial z_{FL}} + F_{s_{FR}}\frac{\partial \delta l_{FR}}{\partial z_{FL}} + F_{s_{RL}}\frac{\partial \delta l_{RL}}{\partial z_{FL}} + F_{s_{RR}}\frac{\partial \delta l_{RR}}{\partial z_{FL}} \tag{21}$$

$$\mathbf{Q}^{s}_{\text{exact}}(5,1) = F_{s_{FL}}\frac{\partial \delta l_{FL}}{\partial z_{FR}} + F_{s_{FR}}\frac{\partial \delta l_{FR}}{\partial z_{FR}} + F_{s_{RL}}\frac{\partial \delta l_{RL}}{\partial z_{FR}} + F_{s_{RR}}\frac{\partial \delta l_{RR}}{\partial z_{FR}} \tag{22}$$

$$\mathbf{Q}^{s}_{\text{exact}}(6,1) = F_{s_{FL}}\frac{\partial \delta l_{FL}}{\partial z_{RL}} + F_{s_{FR}}\frac{\partial \delta l_{FR}}{\partial z_{RL}} + F_{s_{RL}}\frac{\partial \delta l_{RL}}{\partial z_{RL}} + F_{s_{RR}}\frac{\partial \delta l_{RR}}{\partial z_{RL}} \tag{23}$$

$$\mathbf{Q}^{s}_{\text{exact}}(7,1) = F_{s_{FL}}\frac{\partial \delta l_{FL}}{\partial z_{RR}} + F_{s_{FR}}\frac{\partial \delta l_{FR}}{\partial z_{RR}} + F_{s_{RL}}\frac{\partial \delta l_{RL}}{\partial z_{RR}} + F_{s_{RR}}\frac{\partial \delta l_{RR}}{\partial z_{RR}} \tag{24}$$

Since the suspensions are independent, the vertical displacement of the wheel centre at a given corner does not influence the suspension deflection at the other corners:

$$\frac{\partial \delta l_i}{\partial z_j} = 0 \quad \text{with } i \neq j \tag{25}$$

Moreover, analysing the mutual dependencies between the partial derivatives, it results Eq. (26):

$$\frac{\partial \delta l_i}{\partial z_i} = -\frac{\partial \delta l_i}{\partial z_G} = -\frac{\partial \delta l_i}{\partial z_{rel\,i}} \tag{26}$$

This is because both terms appearing in Eq. (26), $\frac{\partial \delta l_i}{\partial z_i}$ and $\frac{\partial \delta l_i}{\partial z_G}$, represent the partial derivatives of the suspension deflection with respect to the relative vertical displacement between the chassis and the wheel centre at the i-th corner (in opposite directions and with pitch and roll rate equal to zero).

A further simplification has been introduced by assuming the horizontal distance between the vehicle's centre of gravity and the direction of application of each suspension force to be constant, neglecting its variation due to roll and pitch. Under this assumption, supported by the hypothesis of small angles, the pitch and roll moments, $F_{s_i}\frac{\partial \delta l_i}{\partial \theta}$ and $F_{s_i}\frac{\partial \delta l_i}{\partial \phi}$, due to the reaction of a single suspension F_{s_i} are proportional to the vertical force transmitted to the chassis $F_{s_i}\frac{\partial \delta l_i}{\partial z_G}$, through a constant ratio, resulting:

$$\frac{\partial \delta l_i}{\partial \phi} = a_i\frac{\partial \delta l_i}{\partial z_{CG}} \tag{27}$$

$$\frac{\partial \delta l_i}{\partial \theta} = b_i\frac{\partial \delta l_i}{\partial z_{CG}} \tag{28}$$

Therefore the equations can be rewritten as follows:

$$\mathbf{Q}^{s}_{r}(1,1) = F_{s_{FL}}\frac{\partial \delta l_{FL}}{\partial z_{CG}} + F_{s_{FR}}\frac{\partial \delta l_{FR}}{\partial z_{CG}} + F_{s_{RL}}\frac{\partial \delta l_{RL}}{\partial z_{CG}} + F_{s_{RR}}\frac{\partial \delta l_{RR}}{\partial z_{CG}} \tag{29}$$

$$\mathbf{Q}^{s}_{r}(2,1) = -a_f F_{s_{FL}}\frac{\partial \delta l_{FL}}{\partial z_{CG}} + a_f F_{s_{FR}}\frac{\partial \delta l_{FR}}{\partial z_{CG}} - a_r F_{s_{RL}}\frac{\partial \delta l_{RL}}{\partial z_{CG}} + a_r F_{s_{RR}}\frac{\partial \delta l_{RR}}{\partial z_{CG}} \tag{30}$$

$$\mathbf{Q}^{s}_{r}(3,1) = b_f F_{s_{FL}}\frac{\partial \delta l_{FL}}{\partial z_{CG}} + b_f F_{s_{FR}}\frac{\partial \delta l_{FR}}{\partial z_{CG}} - b_r F_{s_{RL}}\frac{\partial \delta l_{RL}}{\partial z_{CG}} - b_r F_{s_{RR}}\frac{\partial \delta l_{RR}}{\partial z_{CG}} \tag{31}$$

$$\mathbf{Q}^{s}_{r}(4,1) = -F_{s_{FL}}\frac{\partial \delta l_{FL}}{\partial z_{CG}} \tag{32}$$

$$\mathbf{Q}^{s}_{r}(5,1) = -F_{s_{FR}}\frac{\partial \delta l_{FR}}{\partial z_{CG}} \tag{33}$$

$$\mathbf{Q}^{s}_{r}(6,1) = -F_{s_{RL}}\frac{\partial \delta l_{RL}}{\partial z_{CG}} \tag{34}$$

$$\mathbf{Q}^{s}_{r}(7,1) = -F_{s_{RR}}\frac{\partial \delta l_{RR}}{\partial z_{CG}} \tag{35}$$

where a_f and a_r represent the distances between the suspensions' vertical forces and vehicle centre of gravity along the y-axis, evaluated at the front and rear of the vehicle, respectively, while b_f and b_r correspond to the distances along the x-axis. These constant terms are calculated from Eqs. (27) and (28), once the partial derivatives in steady-state equilibrium conditions are defined by solving the velocity problem. The terms $\frac{\partial \delta l_i}{\partial z_{CG}}$ correspond to the motion ratios evaluated at each corner, which depend on the instantaneous constraint configuration and thus have to be defined as function of the current state. In this work, where the steering degree of freedom is not considered, each of these parameters can be identified based on the corresponding suspension deflection and the orientation of the vehicle's z-axis (along which the vehicle-wheel relative displacement is uniquely defined by the suspension deformation) with respect to the global z-axis (in which the translational degrees of freedom are expressed). However, although a fully accurate dependency should also account for roll and pitch, the motion ratios have been analytically expressed as polynomial functions of the respective suspension displacements, in order to limit the nonlinearity of the reduced-order formulation. This simplified assumption provides a good approximation, as confirmed by the Fig. 4, where the second-order polynomial fits are compared with the results of the reference simulation.

It is also worth noting that the polynomial fitting was not performed on the reference simulation data, in order to avoid any influence from the specific choice of operating conditions in the identification process. Instead, it was derived by evaluating the variation of the partial derivatives within a defined domain of independent coordinates, starting from the static equilibrium configuration and applying changes only to the spring deflection, while keeping the chassis orientation and position fixed.

3.2. Reduced mass matrix modelling

The same approach is applied to model the variability of the mass matrix by defining polynomial dependencies between the coefficients of the inverse matrix (to avoid inverting the matrix during the workflow) and the system state variables, also accounting for the symmetry of the resulting matrix. A preliminary analysis of the simulation data was conducted to identify the coefficients that exhibit significant percentage variations and those that have a greater impact on the system response. The latter were quantified by evaluating, in all the simulation domain, the acceleration contribution $\ddot{z}^{j}(i)$ associated with each coefficient, by multiplying it by the corresponding force term:

$$\ddot{z}^{j}(i) = \mathbf{M}^{-1}(i,j)\,\mathbf{Q}(j) \quad \text{with } i \in \{1,\dots,7\} \quad \text{and } j \in \{1,\dots,7\} \tag{36}$$

The coefficients identified through this analysis are those associated with the vertical dynamics of the tyre and the related constraints with the chassis motion:

$$\mathbf{M}^{-1}(i,j) \quad \text{with } i \in \{1,2,3\} \text{ and } j \in \{4,5,6,7\} \tag{37}$$

$$\mathbf{M}^{-1}(j,j) \quad \text{with } j \in \{4,5,6,7\} \tag{38}$$

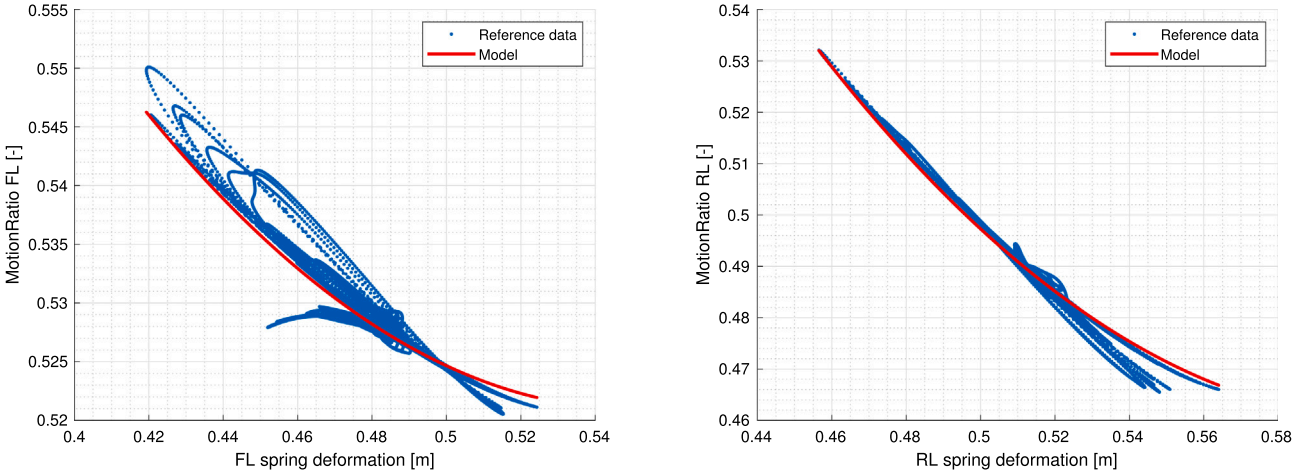

Fig. 4. Motion ratios expressed as function of suspension displacement and compared with simulation data.

Among these, each term related to the j-th wheel centre displacement depends on the suspension displacement at the same corner. This dependence is physically consistent because the suspension displacement defines the current constraints between the sprung and unsprung masses at the corner.

$$\mathbf{M}^{-1}(i,4) = \mathbf{M}^{-1}(4,i) = f_{i,4}(\delta l_{FL}) \quad \text{with } i \in \{1,2,3,4\} \tag{39}$$

$$\mathbf{M}^{-1}(i,5) = \mathbf{M}^{-1}(5,i) = f_{i,5}(\delta l_{FR}) \quad \text{with } i \in \{1,2,3,5\} \tag{40}$$

$$\mathbf{M}^{-1}(i,6) = \mathbf{M}^{-1}(6,i) = f_{i,6}(\delta l_{RL}) \quad \text{with } i \in \{1,2,3,6\} \tag{41}$$

$$\mathbf{M}^{-1}(i,7) = \mathbf{M}^{-1}(7,i) = f_{i,7}(\delta l_{RR}) \quad \text{with } i \in \{1,2,3,7\} \tag{42}$$

As it was already presented for the motion ratios, the polynomial fitting of these dependencies was not performed directly on the reference simulation data, but by computing the mass matrix coefficients, starting from the static equilibrium configuration and applying isolated variations to the suspension displacement, while keeping the chassis position and orientation fixed. The accuracy of the identified second-order polynomial, with respect to the reference simulation data, is illustrated in Fig. 5, which reports the trends of a representative set of mass matrix coefficients as examples. The remaining terms of the mass matrix, whose variations were found to be negligible, were assumed constant and set equal to their steady-state equilibrium values.

3.3. Calculation of dependent variables

Considering the defined dependencies in the dynamic equations and the variables required to calculate the forces acting on the system, the only dependent variables required to calculate are the suspensions' displacements and their time derivatives. The motion ratio concept allows linearizing the dependency between the time derivative of suspension displacement and the relative velocity between chassis and tyre in the corresponding corner:

$$\dot{\delta l}_i = \frac{\partial \delta l_i}{\partial z_{rel_i}} \dot{z}_{rel_i} \tag{43}$$

where:

$$\dot{z}_{rel_{FL}} = \dot{z}_{CG} - a_f\dot{\phi} + b_f\dot{\theta} - \dot{z}_{FL} \tag{44}$$

$$\dot{z}_{rel_{FR}} = \dot{z}_{CG} + a_f\dot{\phi} + b_f\dot{\theta} - \dot{z}_{FR} \tag{45}$$

$$\dot{z}_{rel_{RL}} = \dot{z}_{CG} - a_r\dot{\phi} - b_r\dot{\theta} - \dot{z}_{RL} \tag{46}$$

$$\dot{z}_{rel_{RR}} = \dot{z}_{CG} + a_r\dot{\phi} - b_r\dot{\theta} - \dot{z}_{RR} \tag{47}$$

Unlike the reference model, the simulation workflow of the simplified model does not involve solving the position problem to reconstruct the full set of natural coordinates satisfying the position-level

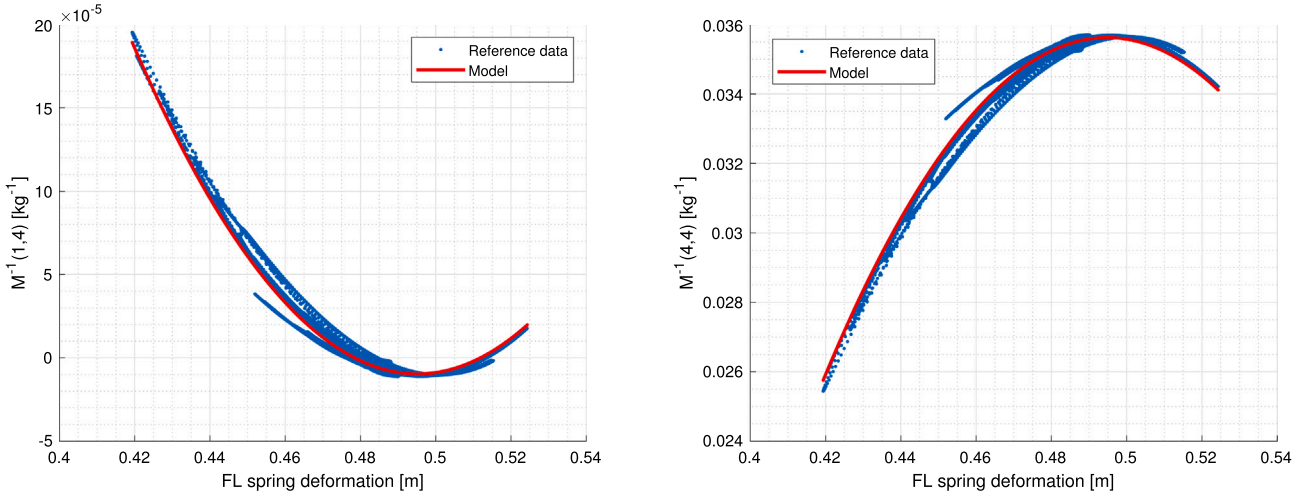

Fig. 5. Mass matrix terms expressed as function of suspension displacement and compared with simulation data.

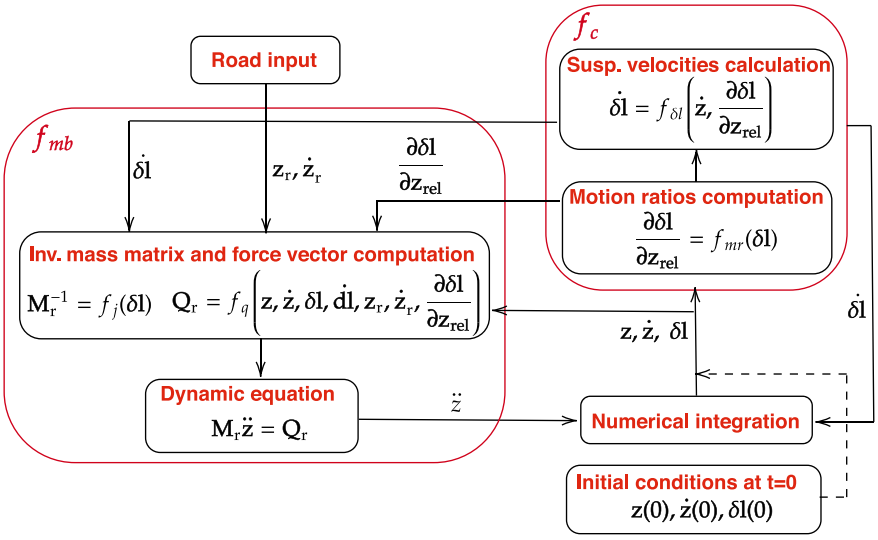

Fig. 6. Schematic workflow of the reduced-order model implementation.

constraints. Instead, the dependent variables at the position level, corresponding to the suspension displacements, are obtained by numerically integrating the suspension deflection velocities reported in Eq. (43).

A schematic description of the workflow of the model is provided in Fig. 6. In this diagram, the terms $\delta\mathbf{l}$, $\dot{\delta}\mathbf{l}$ and $\frac{\partial\delta\mathbf{l}}{\partial z_{rel}}$ represent vectors containing, respectively, the four suspension deflections, their time derivatives, and the four motion ratios evaluated at each corner. The functions f_{mb} and f_c are also represented, as they are employed later in the estimator description presented in Section 4. The first, f_{mb}, represents the set of calculations that receive as input the state variables (both dependent and independent) in terms of position and velocity, as well as the road excitation, and provide as output the vector of accelerations of the independent coordinates. The second, f_c, computes the dependent coordinates from the independent ones at the velocity level. The other functions shown within the individual blocks correspond to f_{mr} and f_j, which represent the polynomial-based computation of the motion ratios and the mass matrix coefficients as functions of the corresponding suspension deflections (Figs. 4 and 5). The function $f_{\delta l}$ refers to Eq. (43) for the four corners, while f_q represents the computation of the reduced force vector terms defined in Eq. (13) as a function of all the state and input variables.

The validation of the simplified model, carried out by comparing its simulation results with those of the full reference model under equivalent operating conditions, confirmed the effectiveness of the proposed approach, which provides a negligible error together with a significant reduction in parameters and computational burden, as shown in Fig. 7. To quantify this agreement, the RMSE and the maximum absolute error among the simulation outputs have been computed for each condition explored by the synthetic dataset, and their mean, standard deviation and maximum value are reported in Table 6. For suspension deflection

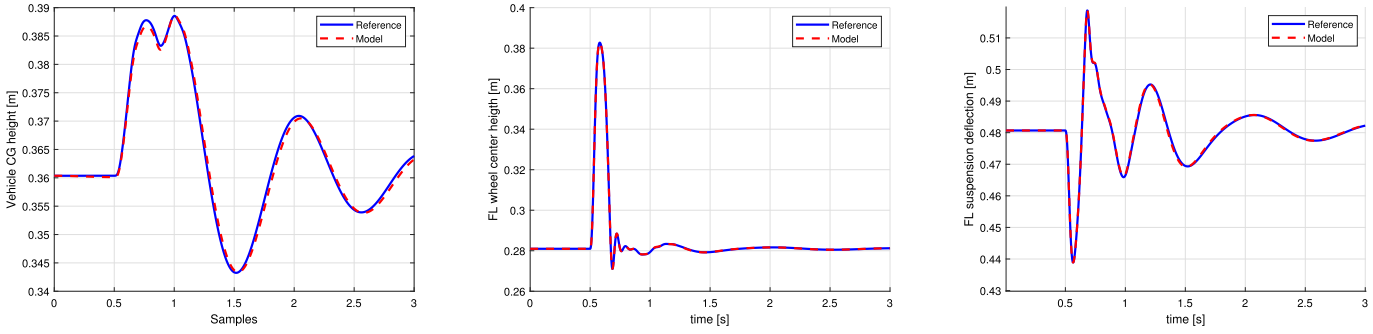

(a) Vehicle center of gravity z_{CG} (b) Front left wheel center z_{FL} (c) Front left δl

Fig. 7. Comparison between reference model results and simplified model.

Table 6
Error metrics evaluated by comparing simplified and reference model outputs across all simulated conditions.

Variable	RMSE			Max absolute error		
	Mean	Std. dev.	Max	Mean	Std. dev.	Max
Centre of gravity [m]	3.84e-04	2.66e-04	1.58e-03	8.12e-04	5.83e-04	3.17e-03
Roll angle [rad]	2.86e-04	2.98e-04	1.01e-03	1.10e-03	1.20e-03	4.27e-03
Pitch angle [rad]	2.25e-04	1.96e-04	9.60e-04	8.82e-04	9.11e-04	4.47e-03
Suspension deflection [m]	2.70e-04	1.87e-04	1.16e-03	9.02e-04	8.62e-04	4.98e-03
Loaded radius [m]	7.56e-05	1.03e-04	7.65e-04	5.63e-04	9.72e-04	5.01e-03

and loaded radius, the reported values refer to the average across the four corners.

4. Estimation infrastructure

The designed estimator has been implemented by employing the Extended Kalman Filter [3] architecture, based on the following workflow, including time-update estimation, performed by using a predictive model:

$$\hat{\mathbf{x}}_k^- = f(\hat{\mathbf{x}}_{k-1}, \mathbf{u}_{k-1}, 0) \tag{48}$$

$$\mathbf{P}_k^- = \mathbf{A_{k-1}}\, \mathbf{P}_{k-1}\, \mathbf{A}_{k-1}^{\mathrm{T}} + \mathbf{Q}_{k-1}^{(n)} \tag{49}$$

and measurement update estimation performing the correction based on the error with respect to instantaneous measurements:

$$\mathbf{K_k} = \mathbf{P}_k^-\, \mathbf{H}_k{}^{\mathrm{T}} (\mathbf{H}_k\, \mathbf{P}_k^- \mathbf{H}_k^{\mathrm{T}} + \mathbf{R}_k^{(n)})^{-1} \tag{50}$$

$$\hat{\mathbf{x}}_k = \hat{\mathbf{x}}_k^- + \mathbf{K_k}(\mathbf{y}_k - \mathbf{h}(\hat{\mathbf{x}}_k^-)) \tag{51}$$

$$\mathbf{P}_k = (\mathbf{I} - \mathbf{K_k}\, \mathbf{H}_k)\, \mathbf{P}_k^- \tag{52}$$

where $\mathbf{R}_k^{(n)}$ and $\mathbf{Q}_{k-1}^{(n)}$ are set to constant values in this work, in order to avoid unnecessarily complicating the formulation. The other terms appearing in Eqs. (48)–(51) are described in the list of symbols reported in Table 7. More detailed information about the Extended Kalman Filter implementation can be found in the cited literature [3,35,36]. It is important to clarify that the choice of the Extended Kalman Filter represents only one possible estimation architecture that can be implemented within the proposed virtual sensing logic. This implementation has been adopted as a representative and computationally efficient solution to validate the proposed approach, while the investigation and comparison of alternative observer architectures will be addressed in future developments.

The state variables characterizing the vector $\hat{\mathbf{x}}_k$ correspond to the independent coordinates of the used 7-dof vehicle model $\{\mathbf{z}\}_k$, the suspension displacements $\{\boldsymbol{\delta l}\}_k$ and the heights of the tyre contact points $\{\mathbf{z}_r\}_k$. While in the previous simulations these last quantities were provided as input variables, in the estimator they must be estimated in real-time. The state vector also includes the time derivatives of the reported quantities.

$$\hat{\mathbf{x}}_k = \begin{pmatrix} \{\dot{\mathbf{z}}\}_k \\ \{\dot{\boldsymbol{\delta l}}\}_k \\ \{\dot{\mathbf{z}}_r\}_k \\ \{\mathbf{z}\}_k \\ \{\boldsymbol{\delta l}\}_k \\ \{\mathbf{z}_r\}_k \end{pmatrix} \quad \{\mathbf{z}\}_k = \begin{pmatrix} z_{CG} \\ \phi \\ \theta \\ z_{FL} \\ z_{FR} \\ z_{RL} \\ z_{RR} \end{pmatrix} \quad \{\boldsymbol{\delta l}\}_k = \begin{pmatrix} \delta l_{FL} \\ \delta l_{FR} \\ \delta l_{RL} \\ \delta l_{RR} \end{pmatrix} \quad \{\mathbf{z}_r\}_k = \begin{pmatrix} z_{r_{FL}} \\ z_{r_{FR}} \\ z_{r_{RL}} \\ z_{r_{RR}} \end{pmatrix} \tag{53}$$

Consistent with previous works integrating multibody models and Kalman Filters [37,38], the time-update and measurement-update equations are implemented using different time steps to account for the sampling rate of the available signals (250 Hz). Specifically, the model time update is performed with a time step of 1 ms, while the measurement update is applied every four model iterations.

Table 7
List of symbols.

Symbol	Definition
$\hat{\mathbf{x}}_k^-$	a-priori state estimation performed at the instant k
$\mathbf{u}_{k-1}$	model input vector at the instant $k-1$
$\mathbf{A_{k-1}}$	Jacobian matrix of the model function defined at the instant $k-1$
$\mathbf{Q}_{k-1}^{(n)}$	covariance matrix of the process noise defined at the instant $k-1$
$\mathbf{P}_k^-$	covariance matrix of the a-priori estimation error at the instant k
$\mathbf{H}_k$	Jacobian matrix of the measurement function defined at the instant k
$\mathbf{K_k}$	Kalman filter gain defined at the instant k
$\mathbf{R}_k^{(n)}$	covariance matrix of the measurement noise defined at the instant k
$\mathbf{y}_k$	vector of measurement signals at the instant k
$\hat{\mathbf{x}}_k$	a-posteriori state estimation performed at the instant k
$\mathbf{P}_k$	covariance matrix of the a-posteriori estimation error at the instant k

4.1. Model-based time-update equations

The first step of the EKF workflow consists of a prediction of the state time evolution from the estimated state at the previous instant. In this case, the update of the vehicle state variables is managed by the previously designed reduced-order model. The second-order time derivatives of the degrees of freedom are calculated as functions of all the state variables (Eq. 54), based on the reduced dynamic equations (Eq. 12). The relationship between suspension displacements and independent coordinates in velocity level, reported at Eq. (43), is employed to compute the time derivatives $\{\dot{\boldsymbol{\delta l}}\}_k^-$, also accounting for the dependency between motion ratios and suspension displacements (Eq. 55). Unlike in the simulations used to generate the synthetic dataset described in Section 2, where a Runge–Kutta trapezoidal integrator was employed, the estimator adopts a forward Euler integration method, which avoids the iterative computation required by implicit methods and, therefore, reduces the computational cost. Although Euler integration is less accurate and may lead to error accumulation in open-loop simulations, in this case, the Kalman Filter correction step aims to compensate for such approximation errors introduced by the integrator, since it is used only within the time-update phase.

$$\{\ddot{\mathbf{z}}\}_{k-1} = f_{mb}(\{\dot{\mathbf{z}}\}_{k-1}, \{\dot{\boldsymbol{\delta l}}\}_{k-1}, \{\dot{\mathbf{z}}_r\}_{k-1}, \{\mathbf{z}\}_{k-1}, \{\boldsymbol{\delta l}\}_{k-1}, \{\mathbf{z}_r\}_{k-1}) \tag{54}$$

$$\{\dot{\boldsymbol{\delta l}}\}_k^- = f_c(\{\dot{\mathbf{z}}\}_k^-, \{\boldsymbol{\delta l}\}_k^-) \tag{55}$$

$$\begin{pmatrix} \{\dot{\mathbf{z}}\}_k^- \\ \{\mathbf{z}\}_k^- \\ \{\boldsymbol{\delta l}\}_k^- \\ \{\mathbf{z}_r\}_k^- \end{pmatrix} = \begin{pmatrix} \{\dot{\mathbf{z}}\}_{k-1} \\ \{\mathbf{z}\}_{k-1} \\ \{\boldsymbol{\delta l}\}_{k-1} \\ \{\mathbf{z}_r\}_{k-1} \end{pmatrix} + \Delta t \begin{pmatrix} \{\ddot{\mathbf{z}}\}_{k-1} \\ \{\dot{\mathbf{z}}\}_{k-1} \\ \{\dot{\boldsymbol{\delta l}}\}_{k-1} \\ \{\dot{\mathbf{z}}_r\}_{k-1} \end{pmatrix} \tag{56}$$

The road height time derivative is updated considering the loaded radius variation as a random-walk variable, whose value is considered to be equal to that at the previous instant, with an uncertainty defined by the tuning of the process noise matrix. Therefore the time derivatives of the contact point heights are supposed equal to the wheel centre vertical velocities:

$$\{\dot{\mathbf{z}}_r\}_k^- = \{\dot{\mathbf{z}}\}_k^- \tag{57}$$

4.2. Measurement-update equations

As previously mentioned, the measurement correction has been tested with two kinds of sensor configurations: the first one only including IMU signals, and the second one with additional suspension displacement measurements.

In the measurement equations, which define the relationship between the state vector and the measured quantities, the IMU accelerations are modelled as the chassis accelerations computed from the state variables using the dynamic equations of the vehicle model, expressed in the vehicle reference frame and including gravity compensation.

$$\mathbf{a}_{IMU}(\mathbf{x}_k^-) = \mathbf{R}_{\mathrm{rot}}(\phi, \theta) \begin{pmatrix} 0 \\ 0 \\ \ddot{z}_{CG} + g \end{pmatrix} \tag{58}$$

It is important to underline that the first (longitudinal) component of the computed acceleration vector $\mathbf{a}_{IMU}(\mathbf{x}_k^-)$ is not included in the measurement update. This is because, in real operating conditions, the longitudinal acceleration is heavily influenced by longitudinal contact forces, which are not currently modelled and can be much larger than

lateral forces, especially since the vehicle is assumed to move in a straight line over obstacles symmetric with respect to the wheel plane. The longitudinal acceleration measurement will be included in future developments, where its role will be specifically to estimate the longitudinal contact forces acting on the vehicle. Conversely, the lateral component is retained in the measurement vector because it is essential to have observability of roll motion variations caused by impacts on one side of the vehicle.

Still consistent with the IMU measurement principles, the angular velocities are defined as the time derivatives of the pitch and roll angles, rotated into the local reference frame according to the Euler angle convention, here represented by the rotation matrix $\mathbf{R}_{\text{rot}}$.

$$\boldsymbol{\omega}_{IMU}(\mathbf{x}_k^-) = \mathbf{R}_{\text{rot}}(\phi,\theta)\begin{pmatrix}0\\ \dot{\theta}\\ 0\end{pmatrix} + \mathbf{R}_{\text{rot}}(\phi)\begin{pmatrix}\dot{\phi}\\ 0\\ 0\end{pmatrix} \tag{59}$$

However, in this configuration, the system is not observable when relying solely on the measurements provided by the aforementioned sensors, as demonstrated by the conducted rank analysis which is going to be described. In this regard, the entire synthetic dataset has been used to compute, at each sampled state, the observability matrix defined as function of the Jacobian matrices of both the model and measurement functions:

$$\mathcal{O} = \begin{pmatrix}\mathbf{H}\\ \mathbf{HA}\\ ..\\ \mathbf{HA}^{n-1}\end{pmatrix}, \tag{60}$$

where n is the dimension of the state vector. The rank of $\mathcal{O}$ must equal n, which in this case is 30, to guarantee observability [3]. In Table 8, the variation range of the computed ranks is reported (Columns 1 and 2) for the configuration employing only the measurements provided by the sensors, showing that the resulting rank is lower than the number of state variables.

A further limitation is that the suspension constraints modelled in the formulation, linking independent and dependent coordinates, are defined only at velocity level and not at position level.

To simultaneously address these limitations, two kinds of artificial measurements have been introduced: a "dummy" measurement of the vehicle's centre of gravity position, and a "constraint measurement" linking the estimated seven degrees of freedom to the estimated suspension deflections.

The first solution involves augmenting the acquired measurement vector with an additional constant component representing the vehicle's centre-of-gravity position under flat-road and steady-state equilibrium conditions. This allows the estimated z_{CG} to converge, after a certain time interval following the passage on the road unevenness, to a constant value, consistent with the physical behaviour of the system. The observability analysis was repeated by adding the centre of gravity height to the measurement functions of both sensing configurations (Columns 3 and 4 of Table 8), showing an increase in rank but still not reaching the full number of state variables.

The second solution consists of adding a measurement function that represents a constraint equation between the dependent and independent coordinates:

$$\{\mathbf{h}^c\}_k = \{\boldsymbol{\delta}\mathbf{l}\}_k^- - \{\boldsymbol{\delta}\mathbf{l}\}_k^c = \mathbf{0}, \qquad \{\boldsymbol{\delta}\mathbf{l}\}_k^c = f_*(\{\mathbf{z}\}_k^-) \tag{61}$$

where $\{\boldsymbol{\delta}\mathbf{l}\}_k^c$ is computed through an analytical formulation enforcing position-level constraints.

The formulation f_* to compute $\{\boldsymbol{\delta}\mathbf{l}\}_k^c$ is parameterised using offline simulation data obtained by solving the multibody position problem over an extended domain. Its polynomial structure ensures a high level of accuracy, while any deviation from the full multibody formulation is accounted for in the measurement noise tuning, associating an uncertainty to these measurement equations. As reported in Columns 1 and 2 of Table 9, adding the constraint equations alone, without the dummy measurement of the centre of gravity, still does not provide full observability in either sensing configuration. When both artificial measurements are included (Columns 3 and 4 of Table 9), the rank of the observability matrix matches the number of state variables. It is important to note, however, that in the sensing configuration without suspension-deflection measurements, the system is not observable under flat road and steady-state conditions (before the obstacle impact induces a variation in the loaded radius), where the observability rank remains equal to 29.

Further dummy measurements are introduced, corresponding to the tyre contact point heights on a flat road, which are set to zero. These are included to ensure that the corresponding state variables converge to zero after the passage over the road irregularity, consistently with the steady-state dummy measurement assigned to the vehicle's centre of gravity position. Furthermore, with these additional artificial measurements, the configuration without suspension deflection always becomes observable. Therefore, the complete measurement function vectors corresponding to the two sensor configurations are defined as follows:

$$\mathbf{h}(\hat{\mathbf{x}}_k^-) = \begin{pmatrix}\mathbf{a}_{IMU}(\mathbf{x}_k^-)\\ \boldsymbol{\omega}_{IMU}(\mathbf{x}_k^-)\\ (z_{CG})_k^-\\ \{\mathbf{h}^c\}_k\\ \{\mathbf{z}_r\}_k^-\end{pmatrix} \qquad \mathbf{h}(\hat{\mathbf{x}}_k^-) = \begin{pmatrix}\mathbf{a}_{IMU}(\mathbf{x}_k^-)\\ \boldsymbol{\omega}_{IMU}(\mathbf{x}_k^-)\\ (z_{CG})_k^-\\ \{\mathbf{h}^c\}_k\\ \{\mathbf{z}_r\}_k^-\\ \{\boldsymbol{\delta}\mathbf{l}\}_k^-\end{pmatrix} \tag{62}$$

4.3. Noise covariance matrices tuning

The measurement noise covariance matrix $\mathbf{R}_k^{(n)}$ is assumed to be diagonal and constant over time. For the sensor measurements, such as IMU accelerations, angular velocities, and suspension deflections (in the second configuration), the corresponding $\mathbf{R}_k^{(n)}$ terms are directly assigned based on the assumed noise levels of the sensors.

On the other hand, the introduced artificial measurements do not originate from physical sensors and thus require a different approach. For the dummy measurements, the associated variances are tuned based on a trade-off between estimation accuracy and noise. Lower variances strengthen their influence on the state estimation, facilitating the convergence to steady-state conditions after transient events (e.g., obstacle traversal), but they also reduce the filter's responsiveness to impulsive variations in road excitation. Conversely, assigning higher variances

Table 8
Rank analysis of the observability matrix when using only sensor measurements and the centre of gravity dummy measurement (required rank: 30).

Measurements	$\begin{pmatrix}\mathbf{a}_{IMU}(\mathbf{x}_k^-)\\ \boldsymbol{\omega}_{IMU}(\mathbf{x}_k^-)\end{pmatrix}$	$\begin{pmatrix}\mathbf{a}_{IMU}(\mathbf{x}_k^-)\\ \boldsymbol{\omega}_{IMU}(\mathbf{x}_k^-)\\ \{\boldsymbol{\delta}\mathbf{l}\}_k^-\end{pmatrix}$	$\begin{pmatrix}\mathbf{a}_{IMU}(\mathbf{x}_k^-)\\ \boldsymbol{\omega}_{IMU}(\mathbf{x}_k^-)\\ (z_{CG})_k^-\end{pmatrix}$	$\begin{pmatrix}\mathbf{a}_{IMU}(\mathbf{x}_k^-)\\ \boldsymbol{\omega}_{IMU}(\mathbf{x}_k^-)\\ (z_{CG})_k^-\\ \{\boldsymbol{\delta}\mathbf{l}\}_k^-\end{pmatrix}$
Rank	19–21	23	21–24	25–26

Table 9
Rank analysis of the observability matrix when using constraint measurements and the full set of artificial measurements (required rank: 30).

Measurements	$\begin{pmatrix}\mathbf{a}_{IMU}(\mathbf{x}_k^-)\\ \boldsymbol{\omega}_{IMU}(\mathbf{x}_k^-)\\ \{\mathbf{h}^c\}_k\end{pmatrix}$	$\begin{pmatrix}\mathbf{a}_{IMU}(\mathbf{x}_k^-)\\ \boldsymbol{\omega}_{IMU}(\mathbf{x}_k^-)\\ \{\mathbf{h}^c\}_k\\ \{\boldsymbol{\delta}\mathbf{l}\}_k^-\end{pmatrix}$	$\begin{pmatrix}\mathbf{a}_{IMU}(\mathbf{x}_k^-)\\ \boldsymbol{\omega}_{IMU}(\mathbf{x}_k^-)\\ (z_{CG})_k^-\\ \{\mathbf{h}^c\}_k\end{pmatrix}$	$\begin{pmatrix}\mathbf{a}_{IMU}(\mathbf{x}_k^-)\\ \boldsymbol{\omega}_{IMU}(\mathbf{x}_k^-)\\ (z_{CG})_k^-\\ \{\mathbf{h}^c\}_k\\ \{\boldsymbol{\delta}\mathbf{l}\}_k^-\end{pmatrix}$
Rank	27–28	28	29–30	30

increases the filter's sensitivity to dynamic changes but results in higher noise levels in the estimated states during steady-state conditions.

For the constraint measurements, the associated variance is set equal to the variance of the error in the analytical formulation of $\{\boldsymbol{\delta l}\}_k^c$ with respect to the full multibody model, computed offline.

The process noise covariance matrix $\mathbf{Q}_{k-1}^{(n)}$ is constant and tuned using the Maximizing Joint Likelihood method [3,10]. In this procedure, the simulation data generated by the reference multibody model are used as the calibration dataset. At each time step, the reference state provided by the simulation at the previous instant, $\mathbf{x}_{k-1}$, is used as input to the reduced-order model to compute the corresponding state prediction $f(\mathbf{x}_{k-1})$. The prediction error is then obtained by comparing this estimate with the state provided by the simulation dataset at the subsequent time instant, $\mathbf{x}_k$, which is considered as the reference updated state. The sample covariance of this prediction error, computed over all the available reference data, defines the process noise covariance matrix $\mathbf{Q}_{k-1}^{(n)}$, which is calculated as:

$$\mathbf{Q}_{k-1}^{(n)} = \frac{1}{N}\sum_{k=1}^{N}\left(\mathbf{x}_k - f(\mathbf{x}_{k-1})\right)\left(\mathbf{x}_k - f(\mathbf{x}_{k-1})\right)^{\mathrm{T}}. \tag{63}$$

However, to provide an extra degree of freedom in tuning, a key parameter is optimized to improve estimator performance. This parameter represents the variance of the loaded radius variation with respect to the previous state, is considered equal for the four tyres and defines the uncertainty related to the update equations of the time derivative of the tyre contact point heights:

$$\sigma^2(\dot{z}_r) = \frac{1}{4}\sum_{i=1}^{4}\frac{1}{N}\sum_{k=1}^{N}(\dot{z}_i(k) - \dot{z}_{r_i}(k)))(\dot{z}_i(k) - \dot{z}_{r_i}(k)))^{\mathrm{T}} \tag{64}$$

This parameter effectively acts as a tuning factor for a low-pass filtering effect on the estimated loaded radius. Increasing the variance enhances the estimator's responsiveness, but introduces more noise in the estimated quantity. In contrast, reducing it filters out high-frequency noise more effectively, at the cost of increased estimation delay during transient dynamics.

5. Results

This section presents a comprehensive analysis of the performance of the estimator, organized into the following main phases:

- Evaluation of estimator accuracy with optimized filter parameters under various operating conditions, including a comparison between the two sensor configurations. Key error metrics assess estimation accuracy for chassis orientation (pitch and roll), tyre-road interaction (contact point and tyre loaded radius), and suspension displacement.
- Analysis of the robustness to modelling uncertainties, by introducing random perturbations to the model parameters used in both time-update and measurement-update functions.
- Sensitivity analysis to examine the impact of filter parameter variations on estimator performance.
- Investigation of the impact of sensor noise levels on estimation accuracy.

5.1. Analysis of overall estimation accuracy with optimized parameters

Figs. 8–10 present direct comparisons between the results of the two estimator configurations and the reference simulation data (Estimator 2 includes suspension deflection measurements). The first figure shows the estimated pitch and suspension displacements, while the others focus on the estimation of tyre-road interaction, displaying contact point height and loaded radius for front and rear tyres for a bump and a pothole excitation respectively. These figures refer to specific operating conditions chosen as representative cases of symmetric excitation. To quantitatively support the findings emerging from the graphical analysis, RMSE values were computed over all simulated conditions, and their mean, maximum values, and standard deviation are reported in Table 10.

As shown in Fig. 8(a), the pitch angle is estimated with high accuracy in both configurations, maintaining an average error on the order of 0.0001 rad over the entire simulation dataset. Regarding the estimation of suspension displacements, the inclusion of direct measurements in Estimator 2 does not improve the estimation accuracy compared to Estimator 1. On the contrary, a slight increase in noise can be observed in Fig. 8(b)–(c) and in the values reported in Table 10, attributable to the high uncertainty of the suspension-deflection sensors. Nevertheless, both estimators achieve RMSE values significantly lower than the modelled sensor-noise standard deviation, demonstrating the filter's effectiveness in enhancing the estimation of this variable compared to its direct measurement.

In the estimation of the tyre–road contact variables shown in Figs. 9 and 10, both estimators exhibit comparable performance. As with suspension displacements, the inclusion of high-noise suspension measurements in Estimator 2 does not lead to a significant improvement in accuracy, as confirmed by the average and maximum RMSE in the estimation of the contact-point height (Table 10). Both estimators show good responsiveness to rapid variations in the road profile, accurately tracking the obstacle shape without significant delay (Figs. 9(a), (d) and 10(a), (d)) and correctly converging to flat-road conditions due to the effect of the dummy measurements. This behaviour, combined with the accurate estimation of suspension dynamics, enables the loaded radius estimation to capture peaks and valleys with low phase lag. However, Fig. 10(b) highlights a recurrent behaviour also observed in other tests: when the loaded radius exceeds the unloaded value and the tyre temporarily loses contact with the road surface, the estimator is unable to follow its variation during the non-contact phase. This

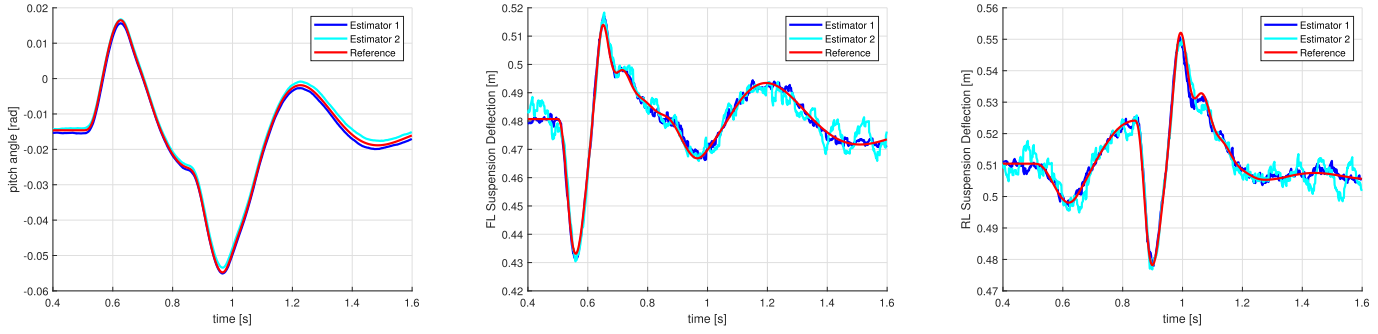

(a) Pitch Angle (b) Front suspension δl (c) Rear suspension δl

Fig. 8. Estimated pitch and suspension displacement compared with reference data.

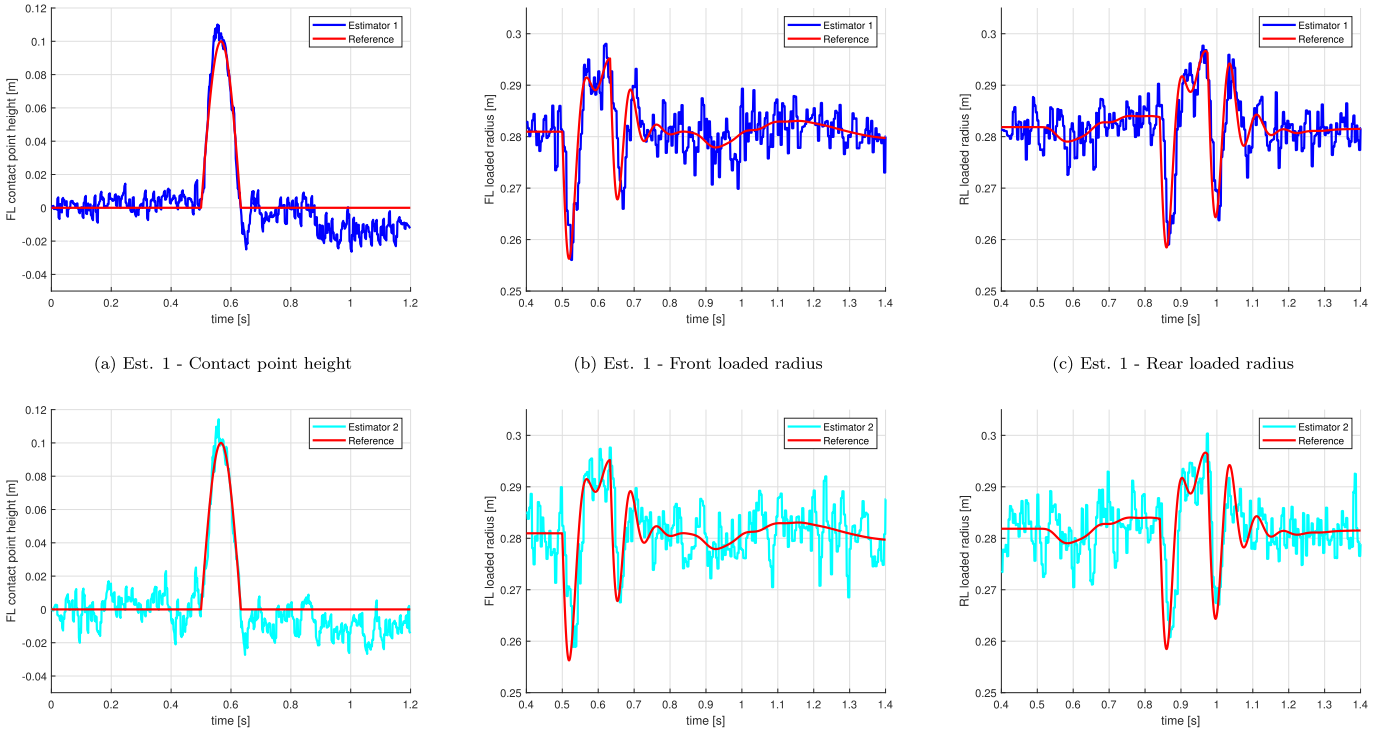

(a) Est. 1 - Contact point height (b) Est. 1 - Front loaded radius (c) Est. 1 - Rear loaded radius

(d) Est. 2 - Contact point height (e) Est. 2 - Front loaded radius (f) Est. 2 - Rear loaded radius

Fig. 9. Estimated contact point heights and loaded radius under symmetric excitations - bump case.

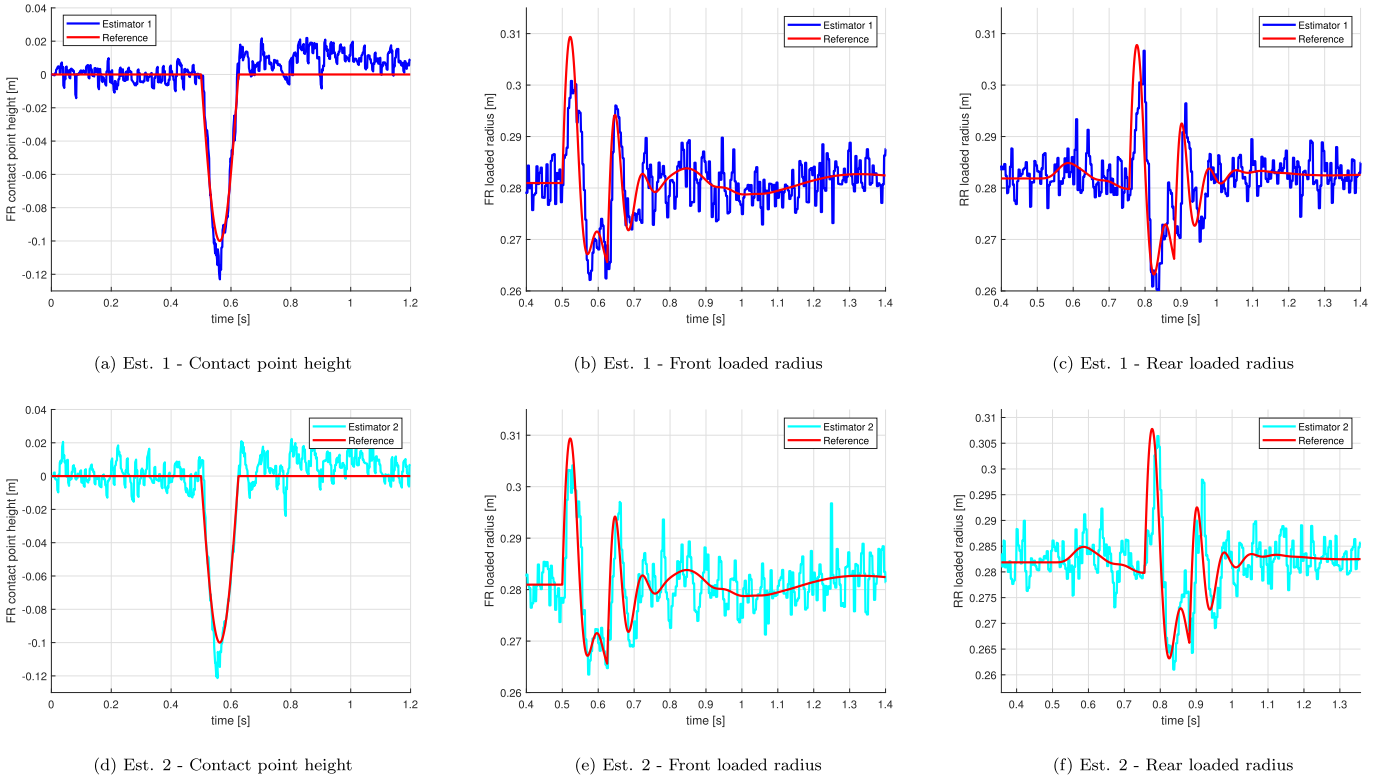

(a) Est. 1 - Contact point height (b) Est. 1 - Front loaded radius (c) Est. 1 - Rear loaded radius

(d) Est. 2 - Contact point height (e) Est. 2 - Front loaded radius (f) Est. 2 - Rear loaded radius

Fig. 10. Estimated contact point heights and loaded radius under symmetric excitations - pothole case.

occurs because the ground-contact force influencing the system dynamics becomes zero for any loaded-radius value greater than the unloaded radius; consequently, the measurement equations cannot provide a precise information on the evolution of this variable until the tyre does not recover the contact. Finally, the estimation of road-contact quantities is inevitably affected by noise, resulting from the combined effect of sensor inaccuracies which, propagated through the observer transfer function to the ground level, lead to an uncertainty on the order

Table 10
RMSE metrics under symmetric excitation conditions.

Variable	Estimator 1			Estimator 2		
	Mean	Std	Max	Mean	Std	Max
Pitch angle [rad]	7.04×10^{-4}	2.93×10^{-4}	1.30×10^{-3}	7.38×10^{-4}	2.72×10^{-4}	1.22×10^{-3}
Suspension deflection [m]	2.08×10^{-3}	3.23×10^{-4}	2.40×10^{-3}	2.20×10^{-3}	1.80×10^{-4}	2.48×10^{-3}
Contact point height [m]	1.13×10^{-2}	3.99×10^{-3}	2.04×10^{-2}	1.28×10^{-2}	4.26×10^{-3}	2.11×10^{-2}
Loaded radius [m]	3.77×10^{-3}	7.69×10^{-4}	5.75×10^{-3}	3.90×10^{-3}	6.92×10^{-4}	5.90×10^{-3}

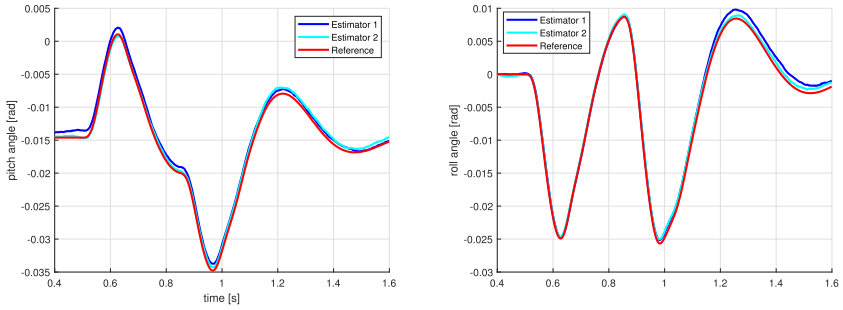

(a) Pitch Angle (b) Roll angle

Fig. 11. Estimated pitch and roll compared with reference data under asymmetric excitation.

Table 11
RMSE metrics under asymmetric excitation conditions.

Variable	Estimator 1			Estimator 2		
	Mean	Std	Max	Mean	Std	Max
Pitch angle [rad]	6.92×10^{-4}	4.46×10^{-4}	1.75×10^{-3}	7.74×10^{-4}	4.14×10^{-4}	1.53×10^{-3}
Roll angle [rad]	9.12×10^{-4}	5.38×10^{-4}	2.21×10^{-3}	9.48×10^{-4}	5.13×10^{-4}	2.11×10^{-3}
Suspension deflection [m]	3.73×10^{-3}	1.15×10^{-3}	5.40×10^{-3}	2.45×10^{-3}	2.47×10^{-4}	2.84×10^{-3}
Contact point height [m]	1.26×10^{-2}	3.80×10^{-3}	1.92×10^{-2}	1.00×10^{-2}	1.99×10^{-3}	1.30×10^{-2}
Loaded radius [m]	3.86×10^{-3}	5.45×10^{-4}	4.96×10^{-3}	3.77×10^{-3}	5.57×10^{-4}	5.04×10^{-3}

of a few millimetres. As will be shown in the sensitivity analysis, this noise can be mitigated by tuning the filter parameters, although this comes at the cost of increased delay and reduced accuracy in capturing high-frequency peaks and valleys.

The inclusion of suspension–deflection measurements becomes crucial when analysing the estimator's performance under asymmetric excitation scenarios. The estimation of pitch and roll performed by the two estimators shows comparable accuracy even in these conditions (Fig. 11), as also confirmed by the error metrics in Table 11. However, as shown in Fig. 12 and confirmed by the trends of RMSE values, the availability of suspension–deflection measurements significantly improves the estimation accuracy of suspension and tyre dynamics. In this regard, under symmetric excitation conditions, the error metrics associated with the two estimators were comparable and, in some cases, slightly lower for Estimator 1 due to the employed high-noise suspension measurements. In contrast, under asymmetric excitations, the RMSE associated with Estimator 1 show significant higher average and maximum values compared to the Estimator 2 for suspension deflection and contact point height.

This occurs because, in symmetric conditions, the absence of significant roll rate variation, captured by the measurements, allows the estimator to recognize a balanced force distribution between the left and right sides of the same axle, enabling the reconstruction of suspension motions even in the absence of direct measurements. On the other hand, under asymmetric excitation, the estimator is no longer able to accurately distinguish the individual irregularities acting on each side of the vehicle (Fig. 12(a) and (d)), since the resulting roll acceleration can be caused by multiple combinations of left and right excitations, making the estimation problem underdetermined. As a result, spikes and significant estimation errors appear not only on the side directly affected by the road disturbance, but also on the opposite side. However, the configuration including suspension deflection sensors, despite the high noise level of the adopted measurements, proves to be robust even under these conditions, without increasing the estimation error range compared to the symmetric simulations.

5.2. Estimator validation under parameters' uncertainty

This analysis aims to assess the robustness of the estimator when inaccuracies in the vehicle model and its parameters are introduced. To this end, a set of random perturbations was applied to the reference parameter set, covering representative sources of modelling uncertainty. Specifically, masses and inertia properties were varied within a range of ±10%, tyre and suspension stiffness and damping within ±15%, and random perturbations were added to the suspension hardpoints with a standard deviation of 0.01m. Five independent combinations of perturbed model parameters were randomly generated and used to run the complete estimation process, each time employing the same filter parameters.

Fig. 13 presents the resulting comparison for roll angle, pitch angle and suspension deflection for the two estimators under one of the perturbed configurations. The results highlight the presence of offsets between the estimated and reference variables, particularly for suspension displacement and pitch angle. This behaviour arises from the fact that, unlike the nominal-case analysis presented in the previous subsection, the reduced-order model and the reference model

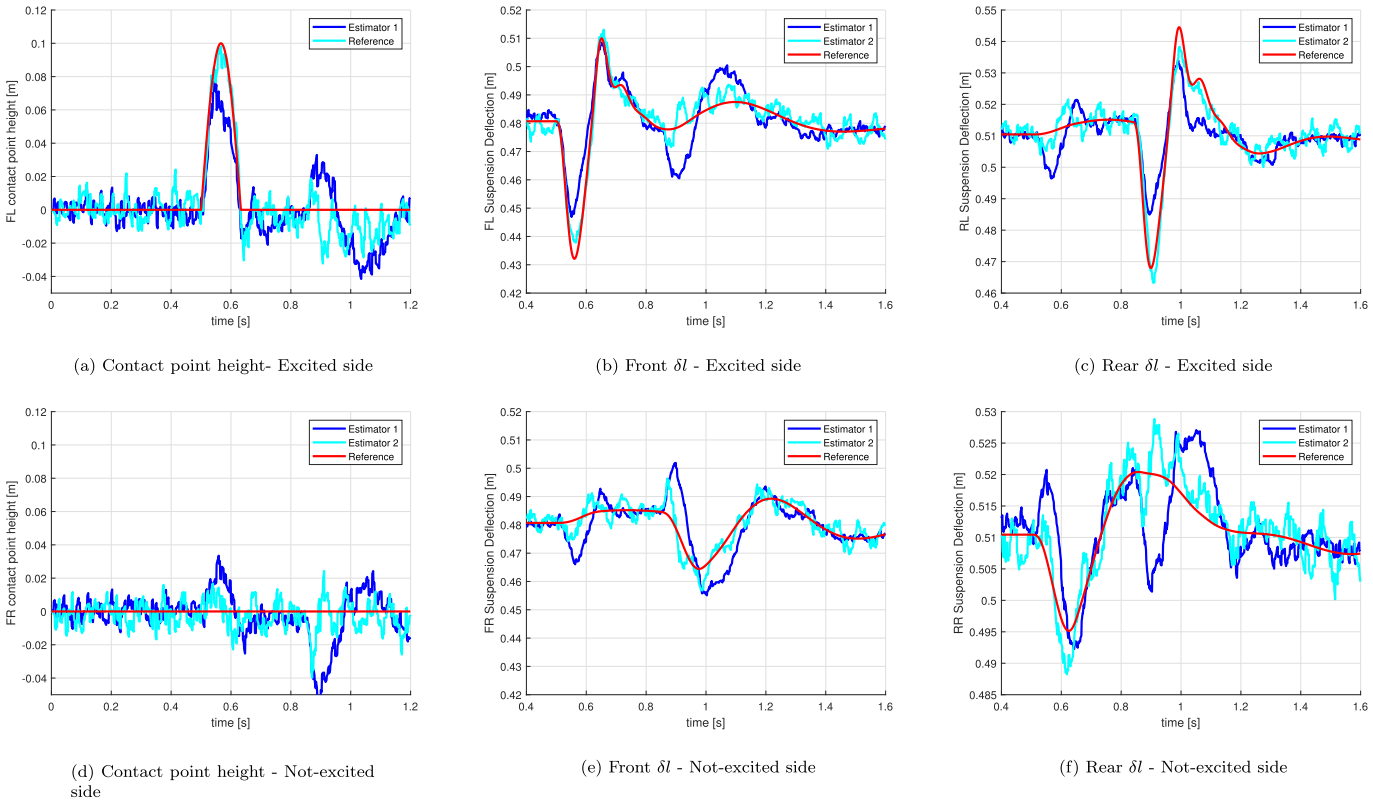

(a) Contact point height- Excited side

(b) Front δl - Excited side

(c) Rear δl - Excited side

(d) Contact point height - Not-excited side

(e) Front δl - Not-excited side

(f) Rear δl - Not-excited side

Fig. 12. Estimated contact point heights and suspensions' deflections under asymmetric excitations.

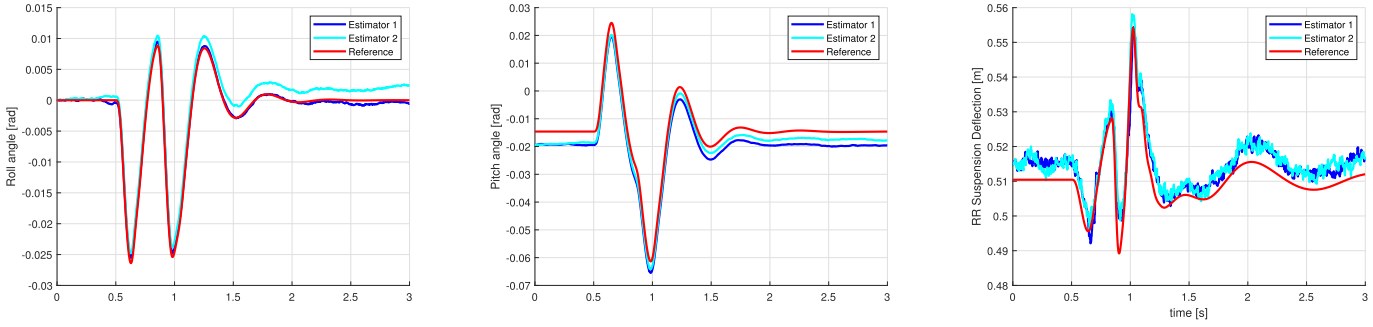

(a) Roll angle

(b) Pitch angle

(c) Front δl

Fig. 13. Estimation of roll angle, pitch angle, and suspension deflection with model parameter perturbations.

do not share the same steady-state equilibrium once parameter perturbations are introduced. Roll angle estimation, however, is not affected by this phenomenon, since its static equilibrium value remains zero.

Despite the presence of these offset components, the robustness of the estimators has been evaluated in terms of the relative evolution of the estimated quantities with respect to their steady-state equilibrium conditions. In this regard, for onboard applications the absolute values of the estimated states are generally less informative than their deviations from equilibrium: in particular, in ride–comfort–oriented control systems, the relevant information is contained primarily in the oscillations around the steady state rather than in the absolute values themselves. Furthermore, this discrepancy also allows verification of the robustness of the algorithm to accelerometer bias, which in this case arises from uncompensated gravitational effects on the accelerometers caused by the non-zero-mean error in the pitch estimation.

Therefore, to quantitatively assess robustness, RMSE values were recomputed over the entire synthetic dataset by evaluating relative estimations by subtracting the corresponding steady-state conditions. The resulting values were computed for each perturbed configuration and are reported in Tables 12 and 13 for symmetric and asymmetric cases, respectively, providing mean, standard deviation, and maximum values.

When evaluated in relative terms, both estimators retain a good level of accuracy under symmetric excitation conditions. This is shown in Fig. 14(a) and (b), where the evolution of pitch angle and suspension deflection reproduces the reference dynamics with good accuracy, as confirmed by the contained increase in RMSE values reported in Table 12. The same is verified for the tyre–road-contact–related variables reported in Fig. 14(c)–(e). In this case, the influence of static equilibrium variation does not lead to a significant offset in the estimation, due to the higher stiffness of the tyre compared to the suspension.

Table 12
RMSE metrics with parameter errors under symmetric excitation conditions.

Variable	Estimator 1			Estimator 2		
	Mean	Std	Max	Mean	Std	Max
Pitch angle [rad]	7.91×10^{-4}	4.13×10^{-4}	2.12×10^{-3}	8.77×10^{-4}	4.45×10^{-4}	2.47×10^{-3}
Suspension deflection [m]	2.42×10^{-3}	6.15×10^{-4}	4.52×10^{-3}	2.36×10^{-3}	3.19×10^{-4}	3.78×10^{-3}
Contact point height [m]	1.27×10^{-2}	4.61×10^{-3}	2.08×10^{-2}	1.32×10^{-2}	4.86×10^{-3}	2.28×10^{-2}
Loaded radius [m]	4.39×10^{-3}	8.83×10^{-4}	7.14×10^{-3}	4.46×10^{-3}	8.15×10^{-4}	6.99×10^{-3}

Table 13
RMSE metrics with parameter errors under asymmetric excitation conditions.

Variable	Estimator 1			Estimator 2		
	Mean	Std	Max	Mean	Std	Max
Pitch angle [rad]	7.55×10^{-4}	4.81×10^{-4}	3.22×10^{-3}	7.26×10^{-4}	4.09×10^{-4}	2.53×10^{-3}
Roll angle [rad]	1.17×10^{-3}	6.86×10^{-4}	3.87×10^{-3}	1.10×10^{-3}	6.45×10^{-4}	3.86×10^{-3}
Suspension deflection [m]	4.11×10^{-3}	1.54×10^{-3}	9.64×10^{-3}	2.65×10^{-3}	4.05×10^{-4}	4.21×10^{-3}
Contact point height [m]	1.38×10^{-2}	4.82×10^{-3}	3.15×10^{-2}	1.08×10^{-2}	2.50×10^{-3}	1.75×10^{-2}
Loaded radius [m]	4.32×10^{-3}	5.53×10^{-4}	5.95×10^{-3}	4.25×10^{-3}	5.31×10^{-4}	5.86×10^{-3}

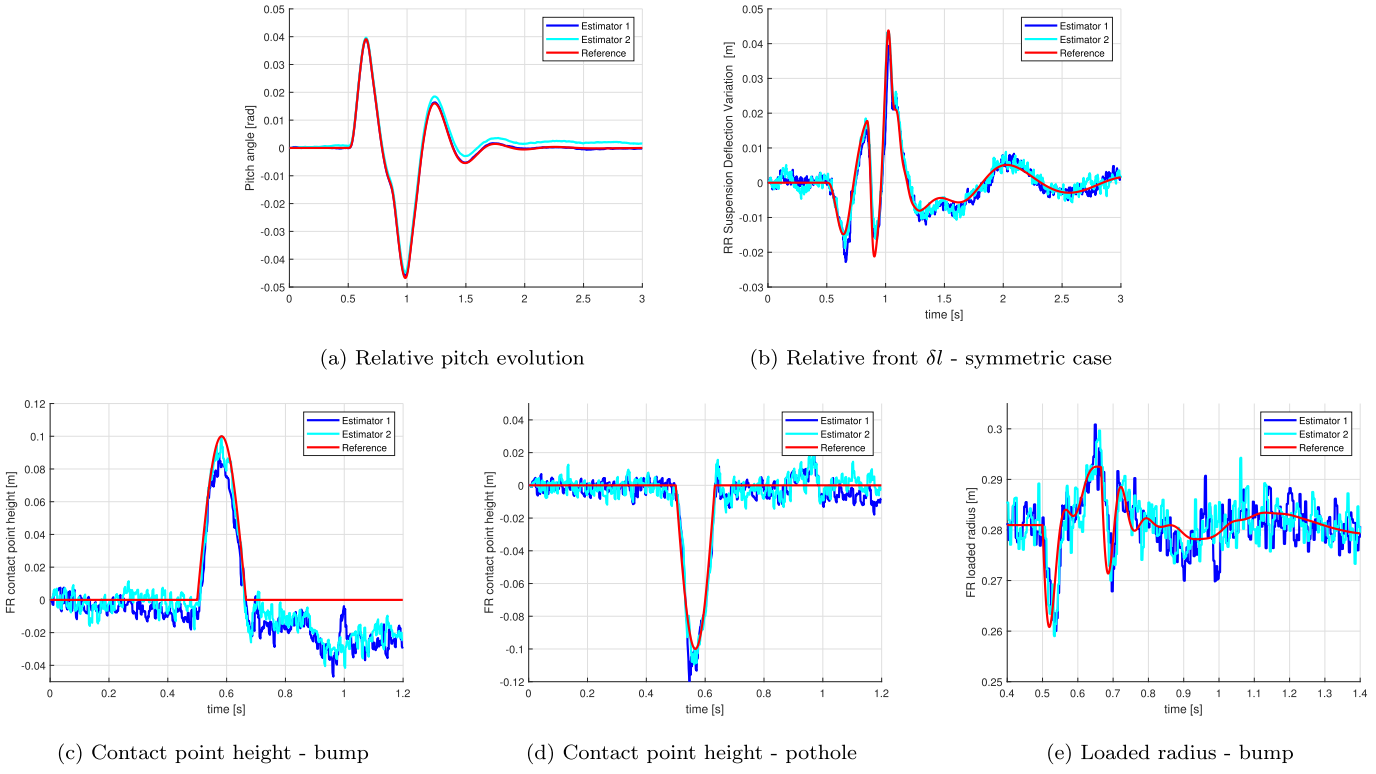

(a) Relative pitch evolution

(b) Relative front δl - symmetric case

(c) Contact point height - bump

(d) Contact point height - pothole

(e) Loaded radius - bump

Fig. 14. Estimation with parameter perturbations under symmetric conditions.

Under asymmetric excitations, the trends observed in the nominal analysis remain valid. As illustrated in Fig. 15, Estimator 1 shows a more pronounced degradation in accuracy, whereas Estimator 2 preserves a more reliable estimation of suspension motion and contact-point height. This is particularly confirmed not only by the increasing average RMSE values but also by the high maximum RMSE computed within the entire dataset. Therefore, this analysis also confirms that the addition of suspension measurements, even with high noise levels, contributes to improving the robustness of the estimator in a wide ride operating domain.

5.3. Sensitivity analysis to filter tuning

One of the objectives of the results analysis is to assess the response of the estimator to variations in the noise covariance tuning, focusing particularly on the previously mentioned parameters, which are crucial in balancing the trade-off between estimation responsiveness to measurement inputs and noise during steady-state conditions, thereby enabling the observer's behaviour to be managed according to application requirements.

Fig. 16 compares estimations obtained by varying the process noise associated with the time-update of the road profile and the results show that the sensitivity of chassis orientation and suspension motion estimates to these parameters is limited. It is worth underlining that the results are shown only for the first estimator configuration; however, the parameter sensitivity is analogous for the second configuration as well. As in previous analyses, a specific operating condition has been selected for graphical comparison, but the observed behaviour is consistent across the entire simulation domain.

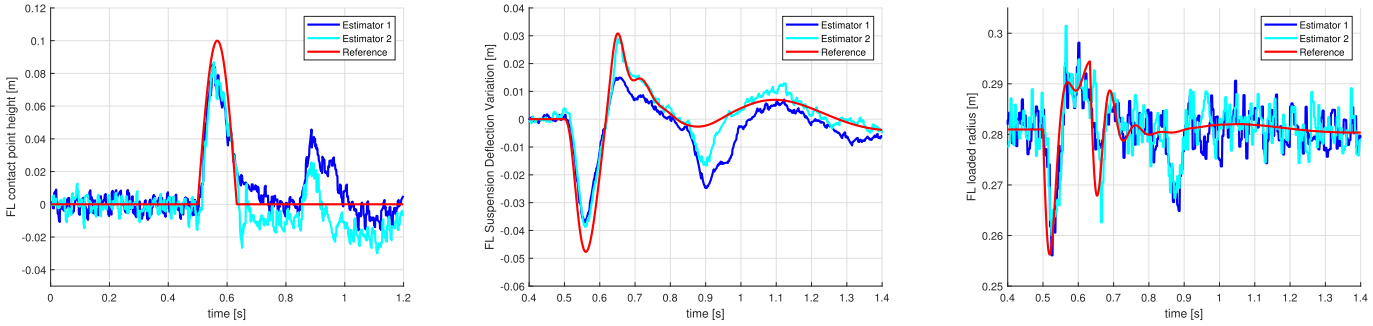

(a) Contact point height - bump (b) Suspension deflection - bump (c) Loaded radius - bump

Fig. 15. Estimation with parameter perturbations under asymmetric conditions.

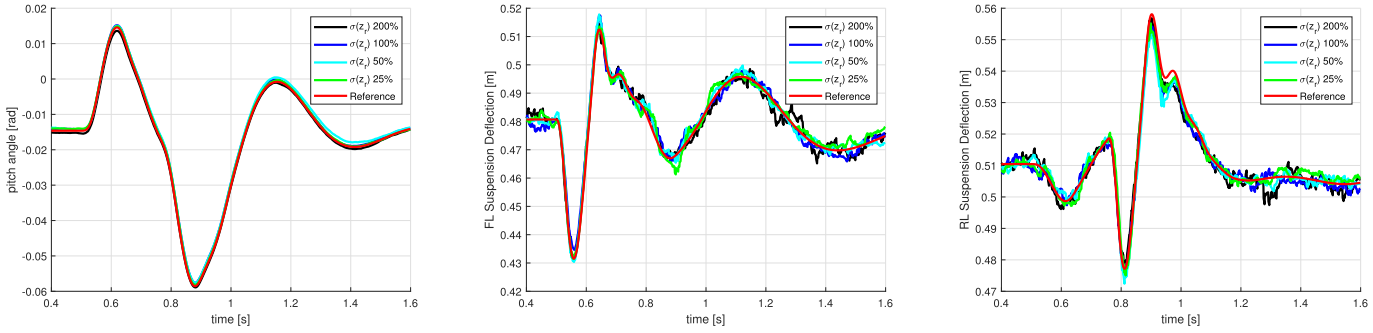

(a) Pitch Angle (b) Front suspension δl (c) Rear suspension δl

Fig. 16. Pitch angle and suspension deflection estimation with variable process noise values.

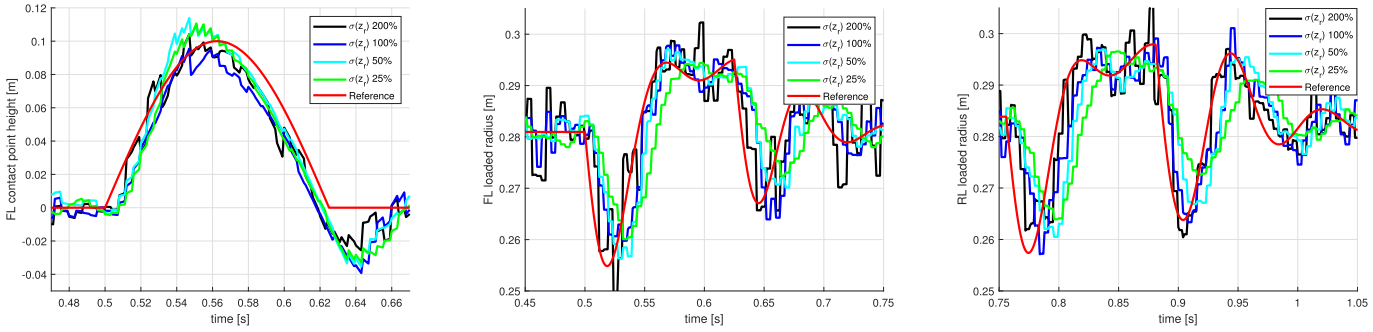

(a) Contact point height - zoomed (b) Front loaded radius - zoomed (c) Rear loaded radius - zoomed

Fig. 17. Tyre-road interaction estimation with variable process noise values.

In contrast, the estimation of the loaded radius is significantly affected by the tuning of this parameter, as it reflects the assumed uncertainty in the hypothesis that this quantity remains constant. As shown in Fig. 17, reducing the assumed uncertainty decreases the noise in the estimation but also reduces the filter's responsiveness. This lower reactivity results in increased estimation errors in both the amplitude and timing of peaks and valleys, in line with the observations discussed in Section 4.3.

On the other hand, while the previous parameter directly affected the loaded radius estimation, adjusting the dummy measurements primarily influences the road contact point estimation, which in turn impacts the loaded radius and suspension deflection. As shown in Fig. 18, the estimation is repeated while progressively reducing the noise associated with these measurements in the $\mathbf{R}_k^{(n)}$ matrix. Lowering this noise makes the road contact point estimation less noisy but also less responsive. In particular, when the noise is excessively reduced, the time history of the contact point height tends to converge too quickly towards zero, failing to track the actual road profile and resulting in an increased estimation error of the loaded radius.

Therefore, the outcomes of this sensitivity analysis highlight that different tuning choices may lead to optimal performance under different operating conditions. This confirms not only the flexibility of the calibration process, allowing optimization to be designed according to the specific objective function to be achieved, whether minimizing estimation variance in steady-state conditions or maximizing accuracy in capturing high-frequency macroscopic oscillations, but also the potential for further improving the estimator's performance through adaptive approaches. In particular, filter parameters could be adjusted online

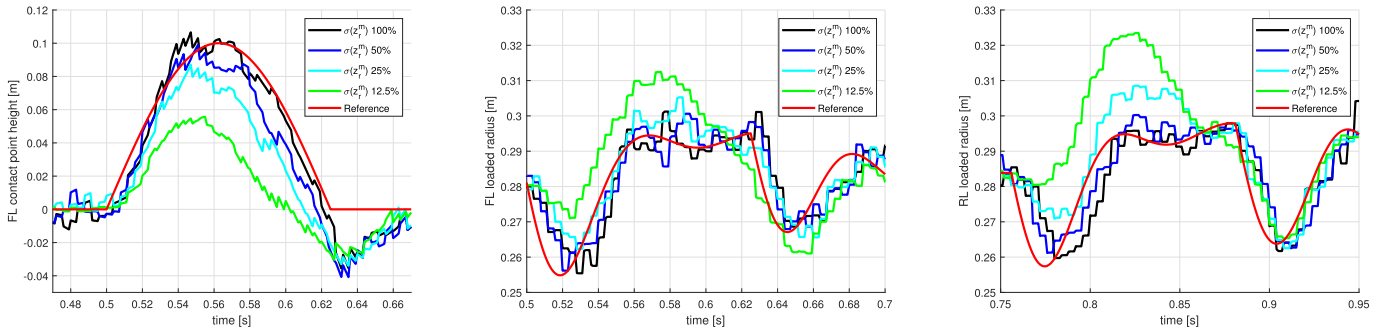

(a) Contact point height - zoomed (b) Front loaded radius - zoomed (c) Rear loaded radius - zoomed

Fig. 18. Tyre-road interaction estimation with variable dummy measurement noise values.

based on the current innovation, enabling the estimator to dynamically balance responsiveness and noise attenuation according to the instantaneous excitation scenario. Such adaptive strategies have already demonstrated their effectiveness in multibody-based estimation frameworks, as reported in [37,39], and represent a promising direction for future developments of the proposed observer.

5.4. Sensitivity analysis to sensor noise

This analysis evaluates how the noise characteristics of the employed sensors affect the estimator's performance. Starting from the baseline configuration reported in Table 5, three different analyses were performed, keeping the model parameters unchanged and modifying only the noise level of the modelled sensors and the corresponding components of the measurement–noise covariance matrix of the EKF:

- The IMU noise (accelerometers and gyroscopes) was reduced by applying scaling factors of 0.5 and 0.25 with respect to the baseline values, and the resulting performance variations were evaluated for Estimator 1.
- The same reductions in IMU noise were then tested on Estimator 2, while keeping the suspension–deflection noise unchanged.
- Finally, the sensitivity of Estimator 2 to suspension–deflection noise was investigated by reducing only the noise of these sensors using the same scaling factors applied in the previous analyses.

For each configuration, the RMSE values were recomputed over the entire synthetic dataset and averaged separately for symmetric and asymmetric excitation conditions, for both Estimator 1 and Estimator 2. The resulting values are summarized in the following Tables 14–16, where, for each state variable of interest, the average RMSE obtained with the baseline noise levels is compared with those corresponding to the two reduced–noise configurations. Graphical comparisons are reported in Figs. 19–21, showing both comparisons between the reference

Table 14
RMSE evaluated for Estimator 1 under different IMU-related noise levels.

Variable	Estimator 1 – symmetric cases			Estimator 1 – asymmetric cases		
	Baseline	$\mathbf{0.5}\,\sigma_{\text{IMU}}$	$\mathbf{0.25}\,\sigma_{\text{IMU}}$	Baseline	$\mathbf{0.5}\,\sigma_{\text{IMU}}$	$\mathbf{0.25}\,\sigma_{\text{IMU}}$
Pitch angle [rad]	7.04×10^{-4}	3.41×10^{-4}	2.63×10^{-4}	6.92×10^{-4}	4.15×10^{-4}	1.72×10^{-4}
Roll angle [rad]				9.12×10^{-4}	4.20×10^{-4}	2.22×10^{-4}
Suspension deflection [m]	2.08×10^{-3}	1.83×10^{-3}	1.88×10^{-3}	3.73×10^{-3}	3.47×10^{-3}	3.40×10^{-3}
Contact point height [m]	1.13×10^{-2}	1.01×10^{-2}	7.89×10^{-3}	1.26×10^{-2}	1.19×10^{-2}	1.11×10^{-2}
Loaded radius [m]	3.77×10^{-3}	3.18×10^{-3}	2.67×10^{-3}	3.86×10^{-3}	3.21×10^{-3}	2.83×10^{-3}

Table 15
RMSE evaluated for Estimator 2 under different IMU-related noise levels.

Variable	Estimator 2 – symmetric cases			Estimator 2 – asymmetric cases		
	Baseline	$\mathbf{0.5}\,\sigma_{\text{IMU}}$	$\mathbf{0.25}\,\sigma_{\text{IMU}}$	Baseline	$\mathbf{0.5}\,\sigma_{\text{IMU}}$	$\mathbf{0.25}\,\sigma_{\text{IMU}}$
Pitch angle [rad]	7.38×10^{-4}	4.63×10^{-4}	1.58×10^{-4}	7.74×10^{-4}	3.79×10^{-4}	2.01×10^{-4}
Roll angle [rad]				9.48×10^{-4}	4.64×10^{-4}	2.01×10^{-4}
Suspension deflection [m]	2.20×10^{-3}	1.99×10^{-3}	1.86×10^{-3}	2.45×10^{-3}	2.24×10^{-3}	2.10×10^{-3}
Contact point height [m]	1.28×10^{-2}	1.03×10^{-2}	8.43×10^{-3}	1.00×10^{-2}	8.69×10^{-3}	7.18×10^{-3}
Loaded radius [m]	3.90×10^{-3}	3.43×10^{-3}	2.94×10^{-3}	3.77×10^{-3}	3.43×10^{-3}	3.06×10^{-3}

Table 16
RMSE evaluated for Estimator 2 under different suspension measurement noise levels.

Variable	Estimator 2 – symmetric cases			Estimator 2 – asymmetric cases		
	Baseline	$\mathbf{0.5}\,\sigma_{\text{susp}}$	$\mathbf{0.25}\,\sigma_{\text{susp}}$	Baseline	$\mathbf{0.5}\,\sigma_{\text{susp}}$	$\mathbf{0.25}\,\sigma_{\text{susp}}$
Pitch angle [rad]	7.38×10^{-4}	7.52×10^{-4}	6.80×10^{-4}	7.74×10^{-4}	6.70×10^{-4}	6.54×10^{-4}
Roll angle [rad]				9.48×10^{-4}	9.97×10^{-4}	9.25×10^{-4}
Suspension deflection [m]	2.20×10^{-3}	1.82×10^{-3}	1.36×10^{-3}	2.45×10^{-3}	1.84×10^{-3}	1.36×10^{-3}
Contact point height [m]	1.28×10^{-2}	1.20×10^{-2}	1.02×10^{-2}	1.00×10^{-2}	8.86×10^{-3}	8.38×10^{-3}
Loaded radius [m]	3.90×10^{-3}	3.86×10^{-3}	3.85×10^{-3}	3.77×10^{-3}	3.83×10^{-3}	3.82×10^{-3}

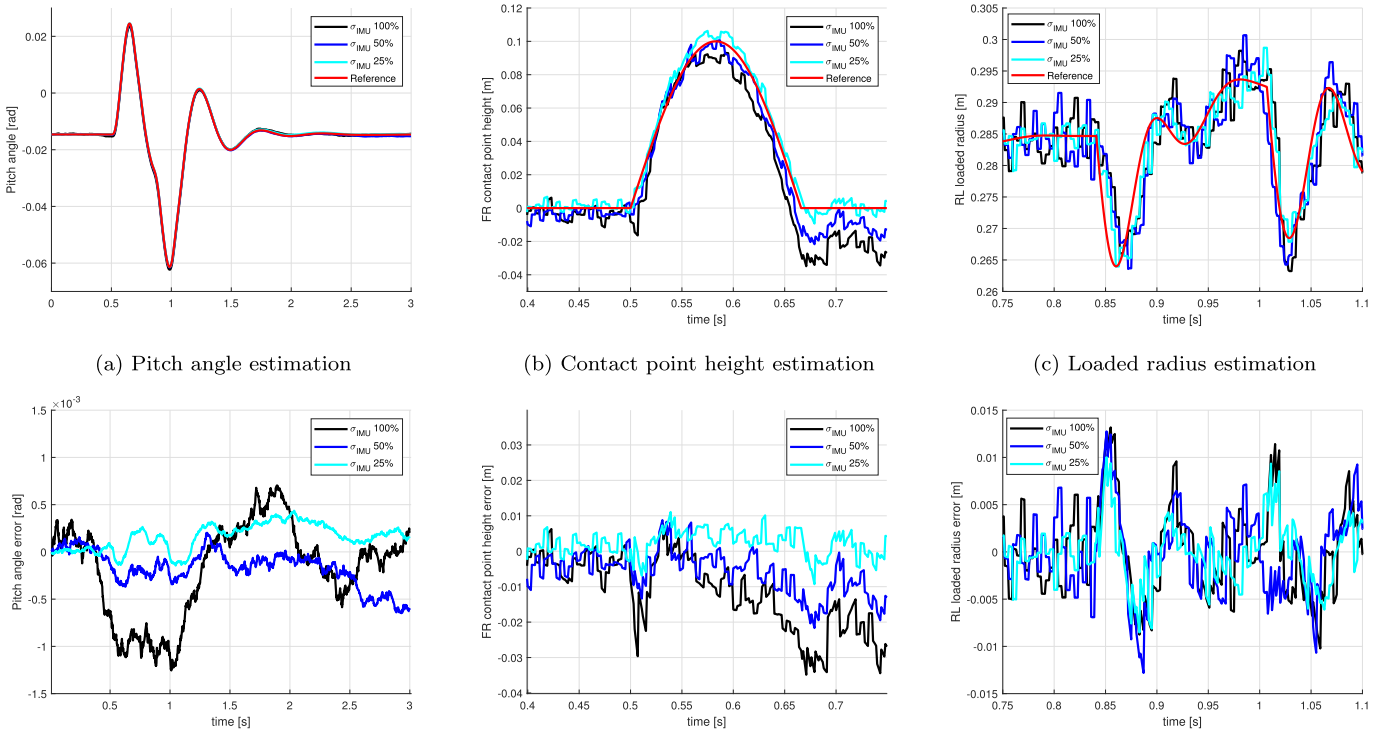

(a) Pitch angle estimation (b) Contact point height estimation (c) Loaded radius estimation

(d) Pitch angle estimation error (e) Contact point height estimation error (f) Loaded radius estimation error

Fig. 19. IMU-related sensors' noise influences on estimation error.

data and the estimations and comparisons of the estimation errors carried out at different noise levels.

Table 14 reports the results of the first analysis, showing that reducing IMU noise has a clear positive impact on the estimation of the Euler angles, as confirmed by Fig. 19(d). On the one hand, this improvement is not highly significant, since even in the baseline (most noisy) configuration, the estimation accuracy remains on the order of 10^{-4} rad. On the other hand, the noise reduction also improves the estimation of the contact point height and the loaded radius, as illustrated in Fig. 19(b), (c), (e) and (f). The same trends are observed for Estimator 2 in Table 15.

However, Estimator 1 continues to exhibit the previously discussed limitations under asymmetric excitations, independently of the applied IMU noise level. Under these conditions, the availability of suspension–deflection measurements becomes crucial, and the benefits of Estimator 2 become more evident, as illustrated in Fig. 20. Tables 14 and 15 further confirm this behaviour: although reducing IMU noise generally improves the accuracy of both estimators, the transition from symmetric to asymmetric excitation has a clearly more negative impact on Estimator 1, with larger positive variations in RMSE compared to those observed in the Estimator 2, especially for suspension deflection and contact point height.

Concerning the third type of analysis, Table 16 shows that increasing the accuracy of the suspension–deflection sensors does not lead to an improvement in the estimation of the chassis orientation. In particular, both pitch and roll RMSE values do not show a monotonic trend with the sensor accuracy, as also evidenced by the estimation–error variations reported in Fig. 21(d). Conversely, the reduction of suspension–deflection noise produces a clear benefit for the estimation of the variables directly provided by these measurements and in the estimation of the tyre-road interaction. As shown in Fig. 21(e) and (f) and confirmed by

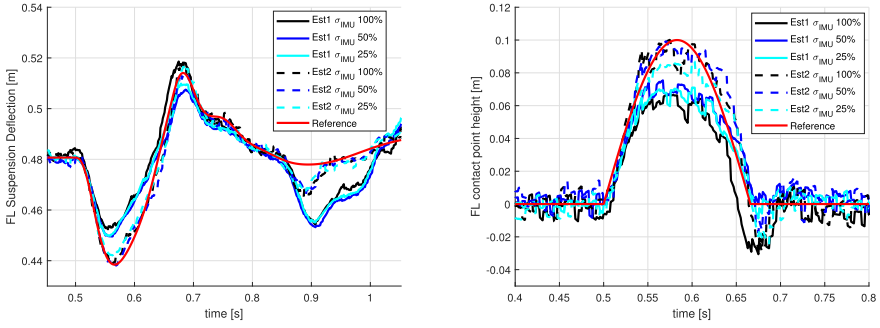

(a) Front δl estimation (b) Contact point height estimation

Fig. 20. Comparison between Estimator 1 and Estimator 2 under asymmetric conditions with different IMU-related sensors' noise.

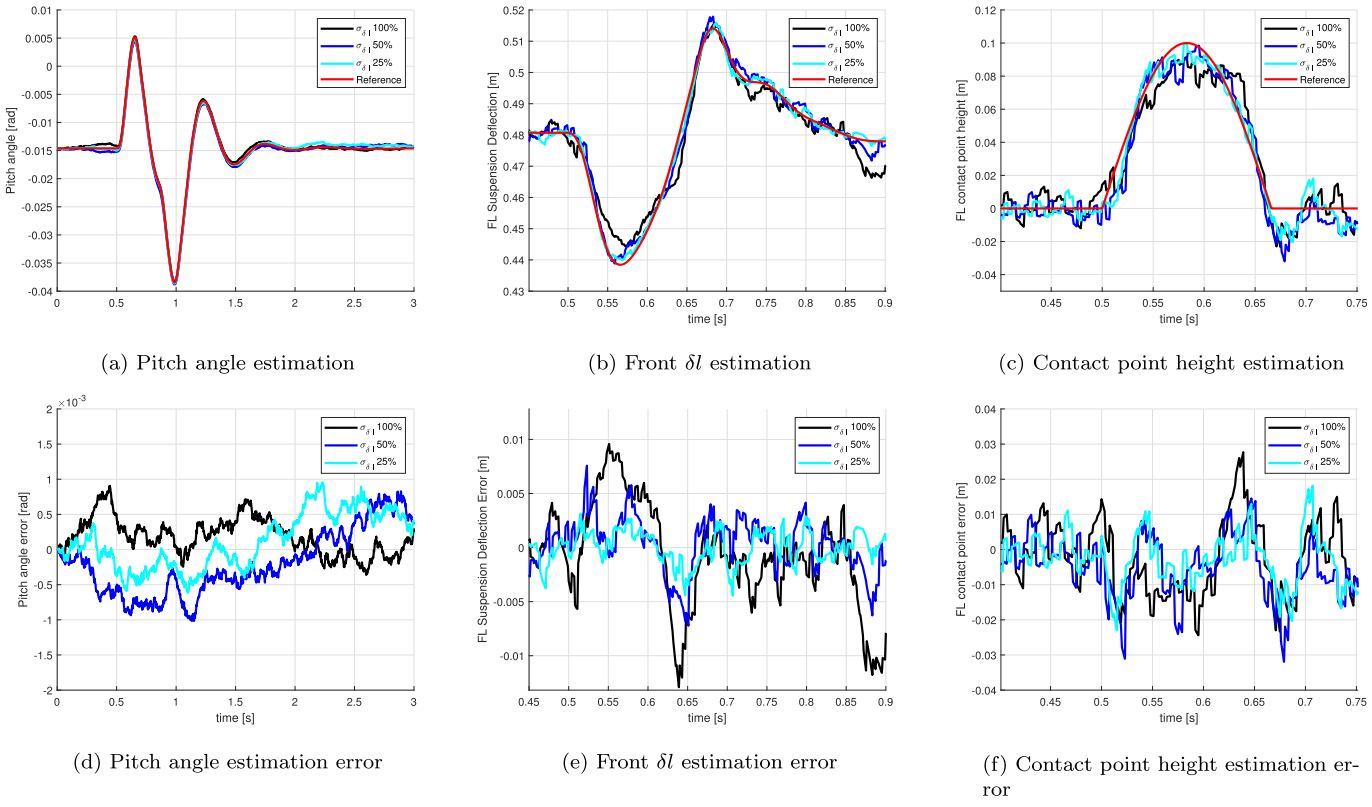

(a) Pitch angle estimation

(b) Front δl estimation

(c) Contact point height estimation

(d) Pitch angle estimation error

(e) Front δl estimation error

(f) Contact point height estimation error

Fig. 21. Suspension sensors' noise influences on estimation error.

the Table 16, the estimation error of the suspension displacement and of the contact point height significantly decreases. The impact on loaded radius however is limited since this estimation mainly depends on the filter parameters and on IMU-related noise levels.

6. Conclusions and further developments

This work presents the development and validation of an Extended Kalman Filter-based observer for on-board estimation of vehicle dynamics during interactions with unknown road unevenness. After generating a simulation dataset using a multibody reference model, a simplified 7-dof vehicle model was designed, validated, and subsequently employed within the estimation process. Two sensor configurations were investigated: one relying solely on IMU signals, and a second that also includes suspension deflection measurements. The observer was tested under various operating conditions, and the analysis of results led to the following conclusions.

The first estimator, which does not rely on suspension deflection measurements, demonstrates satisfactory accuracy under symmetric excitation conditions, where the tyres on the same axle are subjected to equal excitations from the road profile. Consequently, future developments based on this solution, being the most generalizable and compatible with standard vehicle instrumentation, will be limited to this specific operating domain, characterized by negligible roll dynamics. Nevertheless, it is important to highlight that such conditions are approximately representative of the most frequently encountered scenarios in real-world driving. Therefore, despite its constraints, the range of potential applications for this methodology remains significant, making it a promising approach for practical onboard implementation.

To extend the application domain to asymmetric excitations, the second estimator—which incorporates suspension deflection measurements—provides robustness and satisfactory accuracy even under these conditions. Consequently, it represents a more stable and reliable solution across the entire operating range, although it is less generalizable due to its additional required sensors. Furthermore, the robustness analysis conducted under parameter uncertainties confirms this behaviour: while both estimators experience a degradation in accuracy when incorrect model parameters are introduced, the loss of reliability remains limited in symmetric conditions. Under asymmetric excitations, however, Estimator 1 consistently exhibits a markedly larger deterioration, whereas Estimator 2, despite some performance reduction, maintains estimation errors within acceptable bounds, thereby reinforcing the findings obtained in the nominal-case analysis.

A detailed sensitivity analysis of the sensor–noise levels was performed to assess how the quality of the adopted measurements influences the estimation accuracy. In addition, the sensitivity analysis of filter parameters has demonstrated the estimator's calibrability which can be governed by the desired trade-offs between noise rejection and responsiveness.

Overall, this preliminary study has yielded satisfactory results, motivating further developments aimed both at extending the analysis to different vehicle–suspension configurations and at adapting and validating the methodology for practical virtual sensing applications. In this regard, the proposed logic will be tested on various vehicle configurations and suspension layouts to strengthen its generalizability. Furthermore, a trade-off analysis among different estimator architectures will be carried out to identify the optimal solution in terms of estimation accuracy and computational cost, comparing alternative Kalman Filter formulations such as the UKF, the Error-State EKF, and other estimation approaches (e.g., Luenberger observer, Sliding Mode Observer, and alternative stochastic procedures [3,40,41]), in order to assess the impact of the observer architecture on the estimation performance. In addition, adaptive estimators with time-varying covariance matrices will also be investigated to improve accuracy both under flat-road conditions and during road unevenness interactions.

Furthermore, other features will be progressively incorporated into the estimation framework, and successive validation phases will be

undertaken to gradually enhance its suitability for real-world application scenarios. To improve modelling reliability, the approach must account for the tangential forces transmitted to the wheel during road contact and their effects on chassis motions. This will require adopting a reference model with three-dimensional contact model, as well as enhancing the estimation formulation to account for pitch and roll axes that vary based on instantaneous constraint conditions. In addition, the formulation will be adapted to take into account variable steering angles.

Subsequently, more detailed reference models will be considered, using simulation environments with suspension compliance and advanced tyre models. The aim is to evaluate whether the estimator can still capture the vehicle's macroscopic behaviour on the 7 degrees of freedom of interest and to identify the frequency range over which it remains valid. In scenarios where the reference model is not known, both offline and online parameter identification procedures will be tested to estimate model coefficients from simulation data or directly during the estimation process. Subsequently, the estimation methodology will be extended to cover higher-frequency dynamics by incorporating suspension compliances and tyre vibration modes through appropriate reduced-order modelling, to preserve efficiency.

Furthermore, experimental validation will be carried out through outdoor ride tests involving known obstacles [42]. For this activity, the simplified model, implemented according to the methodology developed in this study and potentially enhanced with additional features, will be parameterised through a preliminary indoor test campaign aimed at identifying the key vehicle and tyre properties. In particular, kinematic measurements will be used to identify the motion–ratio variations over the full suspension deflection range, while dynamic tests will allow the estimation of the mass–matrix components by analysing wheel and vehicle accelerations under controlled excitations and different loading conditions, thus enabling calibration across variable suspension deformations.

CRediT authorship contribution statement

Mario Barbaro: Writing – original draft, Validation, Software, Investigation. **Guido Napolitano Dell'Annunziata:** Visualization, Formal analysis, Conceptualization. **Miguel Ángel Naya:** Writing – review & editing, Visualization, Formal analysis. **Antonio J. Rodríguez:** Writing – review & editing, Validation, Software, Formal analysis. **Aleksandr Sakhnevych:** Writing – original draft, Visualization, Supervision, Methodology. **Emilio Sanjurjo:** Validation, Software, Investigation, Conceptualization. **Francisco J. González:** Writing – review & editing, Supervision, Methodology, Conceptualization.

Declaration of competing interest

The authors declare that they have no known competing financial interests or personal relationships that could have appeared to influence the work reported in this paper.

References

[1] Kukkala VK, Tunnell J, Pasricha S, Bradley T. Advanced driver-assistance systems: a path toward autonomous vehicles. IEEE Consum Electron Mag 2018;7(5):18–25.

[2] Ponticelli L, Farroni F, Genovese A, Dell'Annunziata GN, Timpone F, Sakhnevych A. Vehicle state-based control for modern automotive platforms: bridging research and industrial applications. IEEE Access 2025;13:199932–70.

[3] Simon D. Optimal state estimation: kalman, h infinity, and nonlinear approaches. John Wiley & Sons; 2006.

[4] Guo H, Cao D, Chen H, Lv C, Wang H, Yang S. Vehicle dynamic state estimation: state of the art schemes and perspectives. IEEE CAA J Autom Sinica 2018;5(2):418–31.

[5] Liu W, Hua M, Deng Z, Meng Z, Huang Y, Hu C, Song S, Gao L, Liu C, Shuai B, et al. A systematic survey of control techniques and applications in connected and automated vehicles. IEEE Internet Things J 2023;10(24):21892–916.

[6] Farrelly J, Wellstead P. Estimation of vehicle lateral velocity. In: Proceeding of the 1996 IEEE international conference on control applications IEEE international conference on control applications held together with IEEE international symposium on intelligent contro. IEEE; 1996. p. 552–7.

[7] Selmanaj D, Corno M, Panzani G, Savaresi SM. Vehicle sideslip estimation: a kinematic based approach. Control Eng Pract 2017;67:1–12.

[8] Antonov S, Fehn A, Kugi A. Unscented kalman filter for vehicle state estimation. Vehicle Syst Dyn 2011;49(9):1497–520.

[9] Reina G, Paiano M, Blanco-Claraco J-L. Vehicle parameter estimation using a model-based estimator. Mech Syst Signal Process 2017;87:227–41.

[10] Mosconi L, Farroni F, Sakhnevych A, Timpone F, Gerbino FS. Adaptive vehicle dynamics state estimator for onboard automotive applications and performance analysis. Vehicle Syst Dyn 2023;61(12):3244–68.

[11] Carnier S, Corno M, Savaresi SM. Hybrid kinematic-dynamic sideslip and friction estimation. J Dyn Syst Meas Control 2023;145(5):051004.

[12] Oh JJ, Choi SB. Vehicle velocity observer design using 6-d IMU and multiple-observer approach. IEEE Trans Intell Transp Syst 2012;13(4):1865–79.

[13] Villano E, Lenzo B, Sakhnevych A. Cross-combined UKF for vehicle sideslip angle estimation with a modified dugoff tire model: design and experimental results. Meccanica 2021;56:2653–68.

[14] Rodríguez AJ, Sanjurjo E, Pastorino R, Naya MÁ. State, parameter and input observers based on multibody models and kalman filters for vehicle dynamics. Mech Syst Signal Process 2021;155:107544.

[15] Pastorino R, Richiedei D, Cuadrado J, Trevisani A. State estimation using multibody models and non-linear kalman filters. Int J Non-Linear Mech 2013;53:83–90.

[16] Cuadrado J, Vilela D, Iglesias I, Martín A, Peña A. A multibody model to assess the effect of automotive motor in-wheel configuration on vehicle stability and comfort. In: ECCOMAS multibody dynamics; 2013.

[17] Liao Y-W, Borrelli F. An adaptive approach to real-time estimation of vehicle sideslip, road bank angles, and sensor bias. IEEE Trans Veh Technol 2019;68(8):7443–54.

[18] Lingman P, Schmidtbauer B. Road slope and vehicle mass estimation using kalman filtering. Veh Syst Dyn 2002;37(sup1):12–23.

[19] Guiggiani M. The science of vehicle dynamics: handling, braking, and ride of road and race cars. Springer; 2018.

[20] Htike Z, Papaioannou G, Siampis E, Velenis E, Longo S. Minimisation of motion sickness in autonomous vehicles. In: 2020 IEEE intelligent vehicles symposium (IV). IEEE; 2020. p. 1135–40.

[21] Htike Z, Papaioannou G, Siampis E, Velenis E, Longo S. Fundamentals of motion planning for mitigating motion sickness in automated vehicles. IEEE Trans Veh Technol 2021;71(3):2375–84.

[22] Rini G, Menga N, Musci M, Dell'Annunziata GN, Ponticelli L, Sakhnevych A, Timpone F, Bottiglione F. Comprehensive control for autonomous vehicles: from vehicle-to human-centric or from integrated to holistic? IEEE Access 2025;13:188661–86.

[23] Doumiati M, Victorino A, Charara A, Lechner D. Estimation of road profile for vehicle dynamics motion: experimental validation. In: American control conference (ACC); 2011.

[24] Tudon-Martinez JC, Fergani S, Sename O, Morales-Menendez R, Dugard L. Online road profile estimation in automotive vehicles. In: 2014 european control conference (ECC). IEEE; 2014. p. 2370–5.

[25] Singh KB, Arat MA, Taheri S. Literature review and fundamental approaches for vehicle and tire state estimation. Veh Syst Dyn 2019:1643–65.

[26] Takagi K, Morikawa K, Ogawa T, Saburi M. Road environment recognition using on-vehicle lidar. In: 2006 IEEE intelligent vehicles symposium. IEEE; 2006. p. 120–5.

[27] Gargoum S, El-Basyouny K. Automated extraction of road features using lidar data: a review of lidar applications in transportation. In: 2017 4th international conference on transportation information and safety (ICTIS). IEEE; 2017. p. 563–74.

[28] Zhao T, Guo P, He J, Wei Y. A hierarchical scheme of road unevenness perception with lidar for autonomous driving comfort. IEEE Trans Intell Veh 2023;9(1):2439–48.

[29] Guastadisegni G, De Pinto S, Cancelli D, Labianca S, Gonzalez A, Gruber P, Sorniotti A. Ride analysis tools for passenger cars: objective and subjective evaluation techniques and correlation processes–a review. Veh Syst Dyn 2024;62(7):1876–902.

[30] García de Jalón J, Bayo E. Kinematic and dynamic simulation of multibody systems: the real-time challenge. New York: Springer Science & Business Media; 2012.

[31] Cuadrado J, Dopico D, Naya MA, González M. Real-time multibody dynamics and applications. In: Simulation techniques for applied dynamics. Springer; 2008. pp. 247–311.

[32] Cuadrado J, Dopico D, Naya MA, Gonzalez M. Penalty, semi-recursive and hybrid methods for MBS real-time dynamics in the context of structural integrators. Multibody Syst Dyn 2004;12:117–32.

[33] Ascher UM, Petzold LR. Computer methods for ordinary differential equations and differential-algebraic equations. SIAM; 1998.

[34] Schmeitz A, Pacejka H. A semi-empirical, three-dimensional, tyre model for rolling over arbitrary road unevennesses. Veh Syst Dyn 2004;41.

[35] D'Inverno M, Arricale VM, Zanardi A, Frazzoli E, Sakhnevych A, Timpone F. A benchmark study on the model-based estimation of the go-kart side-slip angle. In: Journal of physics: conference series, vol. 2090. IOP Publishing; 2021, p. 012156.

[36] Pyrhönen L, Jaiswal S, Garcia-Agundez A, García Vallejo D, Mikkola A. Linearization-based state-transition model for the discrete extended kalman filter applied to multibody simulations. Multibody Syst Dyn 2023;57(1):55–72.

[37] Rodríguez AJ, Sanjurjo E, Pastorino R, Naya MÁ. Multibody-based input and state observers using adaptive extended kalman filter. Sensors 2021;21(15):5241.
[38] Naya MÁ, Sanjurjo E, Rodríguez AJ, Cuadrado J. Kalman filters based on multibody models: linking simulation and real world. A comprehensive review. Multibody Syst Dyn 2023;58(3):479–521.
[39] Rodríguez AJ, Sanjurjo E, Naya MÁ. An enhanced adaptive kalman filter for multibody model observation. Sensors 2025;25(7):2218.
[40] Zeitz M. The extended luenberger observer for nonlinear systems. Syst Control Lett 1987;9(2):149–56.
[41] Shtessel Y, Edwards C, Fridman L, Levant A, et al. Sliding mode control and observation, vol. 10. Springer; 2014.
[42] Gravante G, Dell'Annunziata GN, Barbaro M, Farroni F. Experimental methodology for tire ride analysis based on outdoor cleat testing. SAE Int J Veh Dyn Stab NVH 2025;9(10–09–03–0023).